Title: 3D geometry of the Lonar impact crater, India, imaged from cultural seismic noise

Authors: Vivek Kumar[1], Shyam S. Rai[1]

Affiliations: [1]Department of Earth and Climate Science, Indian Institute of Science Education & Research Pune, Dr. Homi Bhabha Road, Pune 411008, India

Corresponding author: Vivek Kumar

Email: vivek.seismology@gmail.com

3D geometry of the Lonar impact crater, India, imaged from cultural seismic noise

Vivek Kumar[1], Shyam S. Rai[1]

[1]Department of Earth and Climate Science, Indian Institute of Science Education & Research Pune, Dr. Homi Bhabha Road, Pune 411008, India

Short Title: Velocity model of the Lonar impact crater

Corresponding author: Vivek Kumar

Email: vivek.seismology@gmail.com

Summary

The Lonar impact crater in the Deccan Volcanic Province of India is an excellent analogue for impact-induced structures on the Moon and other terrestrial planets. We present a detailed architecture of the crater using a high-resolution 3-D seismic velocity image to a depth of 1.5 km through the inversion of ambient noise data recorded over 20 broadband seismographs operating around the crater. The ambient noise waveform is dominated by cultural noise in the 1-10 Hz band. The shear wave velocity (Vs) model is created from Rayleigh wave group velocity data with a horizontal resolution of 0.5-1 km in the period range of 0.1-1.2 s. A key feature of the model is a velocity reduction of 10-15 % below the crater compared to outside the ejecta zone. The low-velocity zone below the crater is nearly circular and extends to a depth of ~500 m. This estimated crater's depth is consistent with global depth-diameter scaling relations for simple craters. The basement, with a Vs of more than 2.5 km/s, lies beneath the Deccan basalt, which has a Vs of ~2.4 km/s. These results are consistent with laboratory-measured data from the Lonar crater and borehole data in the western Deccan trap. This study opens a new window for exploring impact craters and sub-basalt structures using high-frequency ambient noise tomography.

Keywords: Seismic tomography, Seismic noise, Impact phenomena

1. Introduction

Impact cratering is a widely recognized process that has affected all planetary bodies with a solid surface (Melosh 1989). Fracturing and brecciation of target rocks and the emplacement of an ejecta blanket around the crater are major outcomes of the impact cratering process (Morgan *et al.* 2013; Osinski *et al.* 2011). The craters are classified as simple or complex based on their shapes and sizes. Simple craters have circular and bowl-shaped depressions with a diameter of less than 2-4 km, while complex craters have large diameters and exhibit central uplifts. The fundamental physics governing the impact processes is the same regardless of the planetary object (Melosh 1989). So far, the Earth has 190 confirmed impact craters (Earth Impact Database; http://passc.net/EarthImpactDatabase/New%20website_05-2018/Index.html), which are the only source of ground truth on impact crater geometry. Knowledge of the geometry of impact craters, such as the depth extent of cracking (or true depth of crater), is essential to understand the strength of the target rocks and the nature of the impactor (Ahrens *et al.* 2002; Robbins *et al.* 2018). Crater's geometry has been mapped using geophysical data (Hanafy *et al.* 2021), especially gravity and magnetic data (reviewed in Gulick *et al.* 2013; Pilkington & Grieve 1992), seismic reflection/refraction, tomographic studies (Christeson *et al.* 2001; Barton *et al.* 2010; Bell *et al.* 2004; Gulick *et al.* 2008), geological methods (Kenkmann *et al.* 2014; Kumar *et al*. 2005), and numerical simulations (Collins *et al.* 2012; Pierazzo & Melosh 2000). However, passive seismology has been used sparingly in imaging the 3-D geometry of impact craters.

The Lonar impact crater is one of the few craters formed entirely in Deccan basalt in western India (Fig. 1). It is a young (570,000 years old) and well-preserved simple crater that provides a unique opportunity to study analogous impact structures on the basaltic surfaces of the Moon and other planets (Fredriksson *et al.* 1973; Maloof *et al.* 2010). The detailed geometry of the Lonar crater also serves as ground truth for global numerical models, e.g., the depth-diameter scaling relation and environmental consequences of impact (Grieve *et al.* 1989; Collins *et al.* 2005). In the present study, the detailed geometry of the Lonar crater is imaged using ambient noise tomography (e.g., Sabra *et al*. 2005; Shapiro *et al*. 2005).

2. The Lonar Crater

The Lonar crater (Fig. 1b) is a bowl-shaped simple impact crater located in the

Maharashtra state, western India (19°58'N, 76°31'E). It was formed at around 570 ka (Jourdan *et al*. 2011) in the Deccan Volcanic Province (DVP), a continental flood basalt province formed due to the interaction of the northward-moving Indian plate and the Reunion hotspot (Morgan 1972). The Deccan basalt has a variable thickness ranging from 200 m to more than 2 km (Harinarayana *et al*. 2007). In the Lonar area, the thickness of the DVP is 600-700 m (Fudali *et al*. 1980). It is believed that the Precambrian granite basement underlies the DVP (Fudali *et al*. 1980; Krishnamurthy 2020). The crater has a rim-to-rim diameter of ~1.8 km, and the maximum elevation of the crater's rim is ~600 m above the mean sea level (Fig. 1b). A continuous blanket of ejecta containing basaltic fragments and impact melt fragments stretches outward to an average distance of 1.35 km from the crater's rim (Fudali *et al*. 1980). The area beyond the ejecta zone is often considered the pre-impact structure. Initially, the crater was thought to be of volcanic origin (La Touche & Christie 1912). The impact origin of the crater was later established based on findings of shock effects (Fredriksson *et al*. 1973; Fudali *et al*.1980). For more detailed geology of the Lonar crater, we refer to Fudali *et al*. (1980) and Maloof *et al*. (2010).

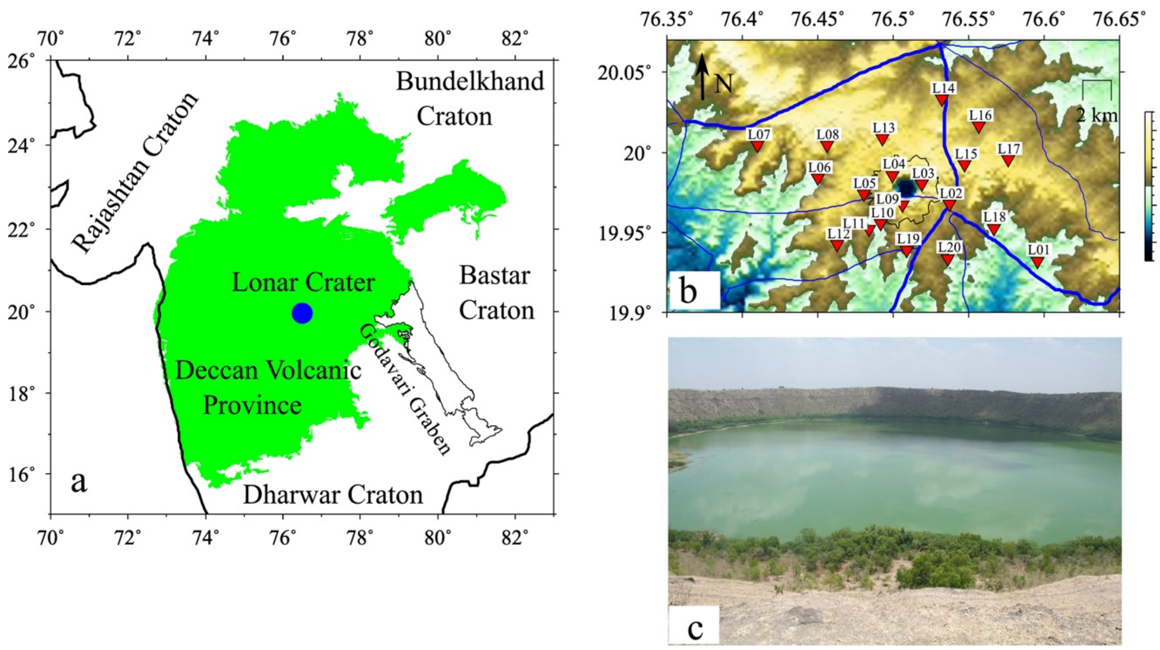

Figure 1: (a) Map of the Indian Shield showing the extent of the Deccan Volcanic Province in the green shade (modified after Kumar *et al*. 2014). The Lonar experimental site is represented as a blue dot. (b) The location of broadband seismographs around the Lonar crater is shown as red inverted triangles. Solid thick blue lines are state motorways, and thin blue lines are local

roadways. The color data in the background represents local topography. (c) A panoramic view of the 1.8 km diameter Lonar Lake caused due to meteoritic impact.

Numerous studies, including drilling, gravity, magnetic, and seismic investigations, have attempted to provide the geometry of the Lonar crater. The early model of the crater, obtained from drill holes up to 310-400 m below the floor level (Fredriksson *et al*. 1973; Fudali *et al*. 1980), shows a sedimentary layer with a maximum thickness of 100 m underlain by brecciated rocks and the crater's depth exceeding 400 m. Rajasekhar & Mishra (2005) and Kiik *et al*. (2020) observed circular/semi-circular gravity and magnetic anomalies and estimated the crater's true depth to be about 500-600 m. A recent study by Sivaram *et al*. (2018), using ambient noise and theoretically computed higher mode surface waves (0.2 to 20 Hz), provided a shear wave velocity model of the crater up to 750 m depth. Due to a low lateral resolution (> 2 km) and a limited vertical extent of the velocity model, they failed to provide the detailed geometry of the crater. Kumar *et al*. (2014) obtained a shear wave velocity model of the top 20-30 m of the ejecta blanket around the crater and imaged impact-related boulders and faults/fractures in the bedrock beneath the crater's rim.

Geophysical methods are important tools for the initial recognition and study of impact craters (reviewed in Pilkington & Grieve 1992). While the potential field methods (e.g., gravity and magnetic methods) are suitable for reconnaissance surveys, seismic methods provide significantly better resolution in impact crater studies (discussed in Morgan *et al*. 2013). With the advances in the processing of ambient noise data (Bensen *et al*. 2007; Schimmel *et al*. 2011), researchers are now able to obtain high-frequency surface waves from the noise waveform and provide high-resolution images of mineral deposits (Chen *et al*. 2021; Li *et al*. 2020), magma sill complexes (Jaxybulatov *et al*. 2014), and glacier structures (Preiswerk & Walter 2018). In this study, we use ambient noise data from broadband stations, previously used by Sivaram *et al*. (2018), around the Lonar crater to generate a 3D shear velocity model with a lateral resolution of 0.5-1 km and a depth of investigation extending to 1.5 km.

3. Data and Method

We use continuous seismic waveform data from 20 broadband seismographs (Table S1) operated by the CSIR-National Geophysical Research Institute (NGRI) between March 2014 and December 2014 around the Lonar crater. Each station, equipped with a Guralp

CMG-3T sensor and REFTEK data logger, recorded waveforms at 100 samples per second with a frequency response from 0.03 to 50 Hz. The shear wave velocity model is obtained in three steps. First, we process the ambient noise data recorded over the network and compute the inter-station group velocity following Bensen *et al*. (2007) and Schimmel *et al*. (2011). These inter-station group velocities are used to generate group velocity maps of the region following the fast marching surface tomography (FMST) approach of Rawlinson (2005). Finally, we invert group velocity dispersion data at each grid point to compute shear wave velocity with depth using the linearized inversion scheme of Herrmann (2013).

3.1 Group velocity dispersion measurements, and noise source characterization

We use the vertical component of the seismic waveform and down sample the data to 20 samples per second. The waveform preprocessing (Bensen *et al*. 2007) involves preparing single-day data, removing mean and trend, correcting for instrument response, and bandpass filtering from 0.2 to 10 Hz. The single-day data is then subjected to time-domain normalization (running absolute mean) and spectral whitening, followed by computing the geometrically normalized cross-correlations (CCGN; Schimmel *et al*. 2011) for all possible raypaths. The daily cross-correlations are further stacked using the time-frequency phase-weighted stack (tf-pws) approach (Schimmel *et al*. 2011) to enhance the signal-to-noise ratio (e.g., Acevedo *et al*. 2019; Kumar *et al*. 2022). We combine the causal and anti-causal parts of the daily cross-correlation and produce symmetric stacked correlations. In Fig. 2, we present stacked cross-correlations with positive lag-time in different frequency ranges between 0.2 and 10 Hz, depicting the emergence of Empirical Green's Functions (EGF) with a high signal-to-noise ratio (SNR) in the 1 to 10 Hz band. The stacked inter-station cross-correlations are used to compute fundamental mode Rayleigh wave group velocity dispersion following the Multiple Filter Technique (MFT) of Dziewonski *et al*. (1969), implemented in Herrmann (2013). An example of group velocity dispersion for a pair of stations is shown in Fig. 3a. From a total of 200 raypaths, we selected 120 raypaths having dispersion data with SNR $\geq$ 5 and an inter-station distance greater than one wavelength in the period range of 0.1 to 1.2 seconds (Fig. 3b and Fig. S1) for further processing.

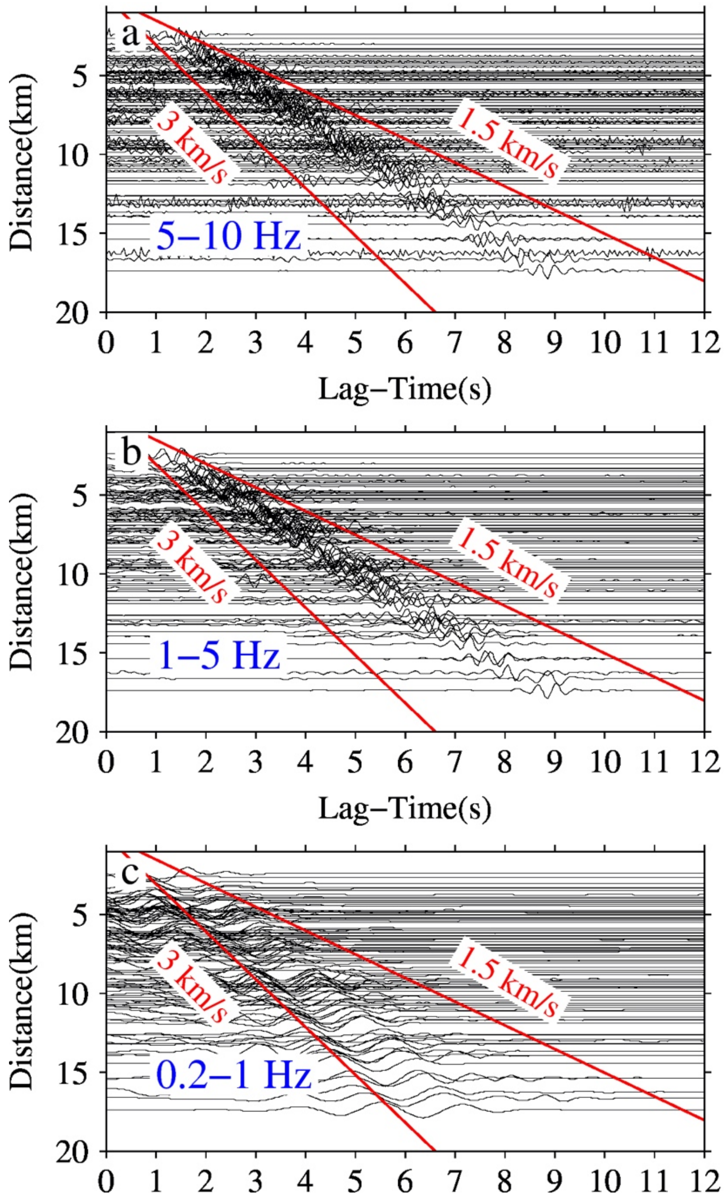

Figure 2: Stacked cross-correlations with positive lag-time plotted with increasing inter-station distances, band pass filtered in the different frequency ranges in (a), (b), and (c). The solid red lines mark the signal window corresponding to velocities between 1.5 km/s and 3 km/s. Areas outside the signal window are considered noise window in SNR calculation.

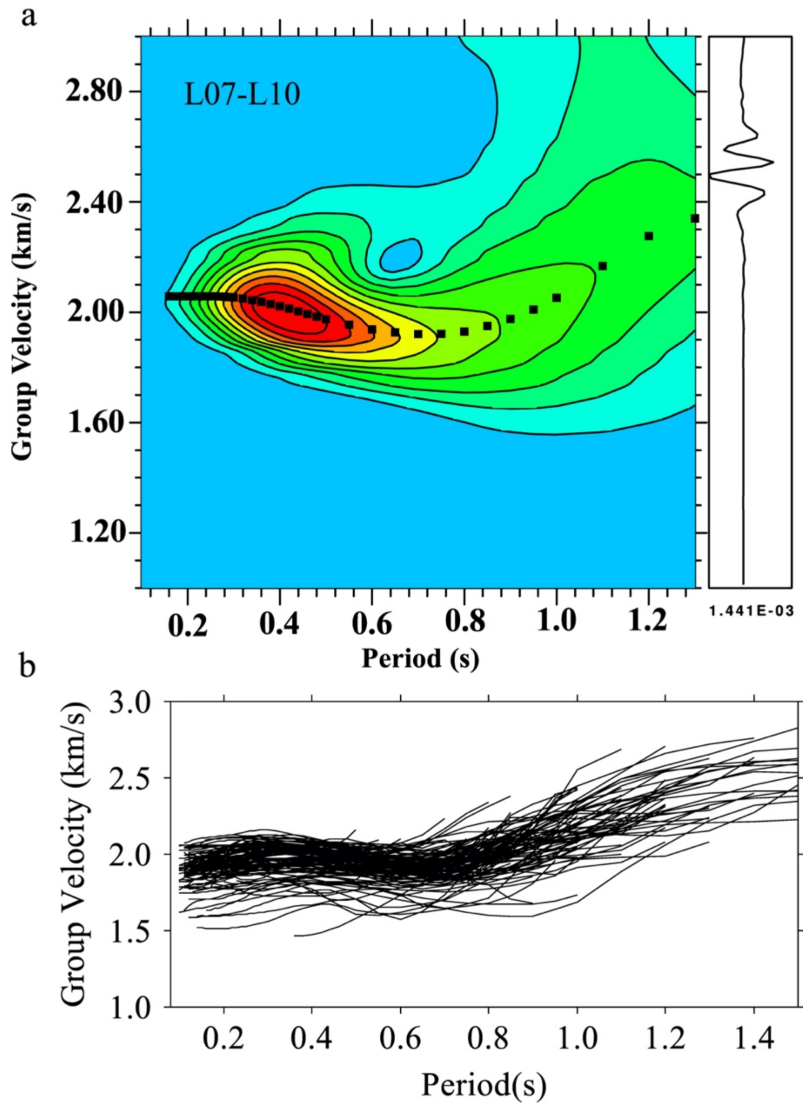

Figure 3: (a) An example group velocity dispersion (black dots) with amplitude contours in the color data obtained by the MFT method implemented in Herrmann (2013). (b) Superposition of all dispersion curves selected in this study.

The dominant frequency range of 1-10 Hz in the computed EGFs of this study corresponds to the short-period noise spectrum (McNamara & Buland 2004). Ambient noise in this band is generated by natural sources such as wind (Johnson *et al*. 2019) or by cultural noise sources (e.g., human activities, traffic, industrial activities, etc.). The cultural noise level has strong diurnal variations, which can be used to distinguish it from natural sources. We used Power Spectral Density (PSD) to quantify seismic noise level (see McNamara & Boaz 2006 for details). Temporal variation of the PSDs for two representative stations, presented in Figs. 4a and b, shows dominant energy from 6 am to 9 pm, possibly due to cultural noise sources in our data. The azimuthal variation of SNR in the causal and anti-causal parts of the

EGFs can be used for locating seismic noise sources (e.g., Yang & Ritzwoller 2008). As shown in Fig. 4c, the EGFs with high SNR are in the N-NW direction, coinciding with the state motorways located just northwest of the network (solid blue lines in Fig. 1b).

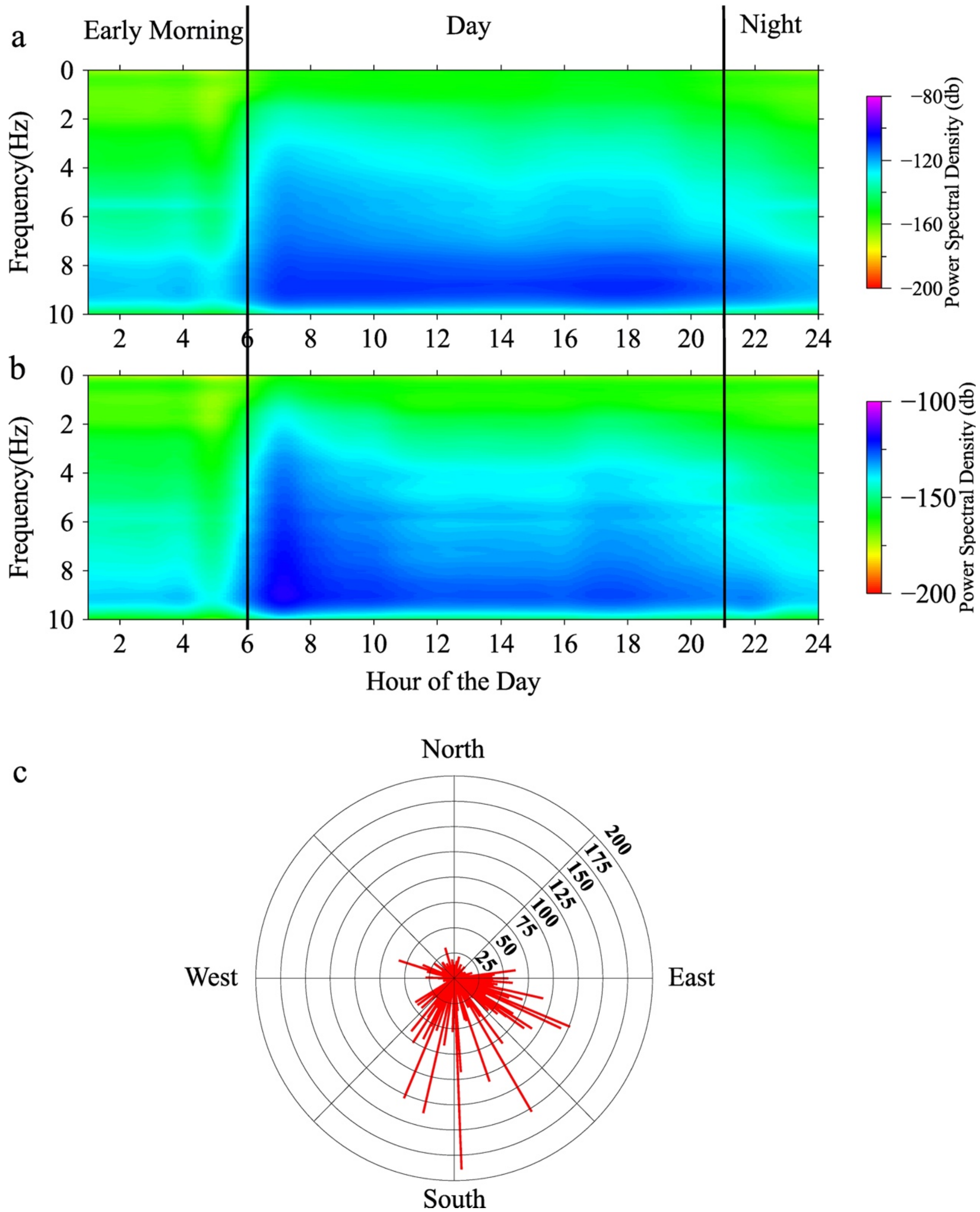

Figure 4: Diurnal variations of noise level at two stations, L03 and L01, in terms of PSD values are shown in (a) and (b). (c) Azimuthal variation of SNR of the computed EGFs. Note that azimuth points towards the receiver.

It should be noted that the method of EGFs retrieval from cross-correlations of ambient noise waveforms rests on the assumption of homogeneous noise source distribution (e.g., Lobkis & Weaver 2001). The temporal and azimuthal variations in noise sources observed in this study (Fig. 4) may introduce biases in dispersion measurements (e.g., Fichtner 2015; Tsai 2009). However, several studies, including real data measurements (e.g., Forment *et al*. 2010; Weaver *et al*. 2009; Yao & van der Hilst 2009), have demonstrated that the measurement error resulting from uneven distribution of noise sources is small (< 1 %), which may be relevant for monitoring studies but has no significant effect on ambient noise tomography. Although it is beyond the scope of this study, recent developments in seismology provide ways to reduce this error through full waveform ambient noise inversions (e.g., Sager *et al*. 2018), computing differential sensitivity kernels (Liu 2020) and coda wave correlations (Colombi *et al*. 2014).

3.2 Group velocity maps

The inter-station group velocity measurements obtained in the previous section are used to generate group velocity maps of the region using an iterative linearized inversion scheme implemented in the Fast Marching Surface Tomography (FMST) package by Rawlinson (2005). The inversion scheme minimises an objective function $\emptyset(\theta)$ which is expressed as

$$\emptyset(\theta) = (g(\theta) - d)^T C_d^{-1} (g(\theta) - d) + \varepsilon(\theta - \theta_0)^T C_\theta^{-1} (\theta - \theta_0) + \eta\, \theta^T D^T D \theta\,, \qquad (1)$$

where d and θ are the data and unknown model parameters, respectively. D is the flatness matrix, C_d and C_θ are data and model covariance matrices, respectively. $g(\theta)$ represents the forward computation of group travel time for the model (θ), which is performed by a grid-based Eikonal solver -the Fast Marching Method (FMM; Rawlinson & Sambridge 2005). The reference velocity model is given by θ_0, which is taken as the mean of average inter-station group velocity measurements. The regularization parameters, denoted as ε (damping) and η (smoothing), are constrained using L-curve tests.

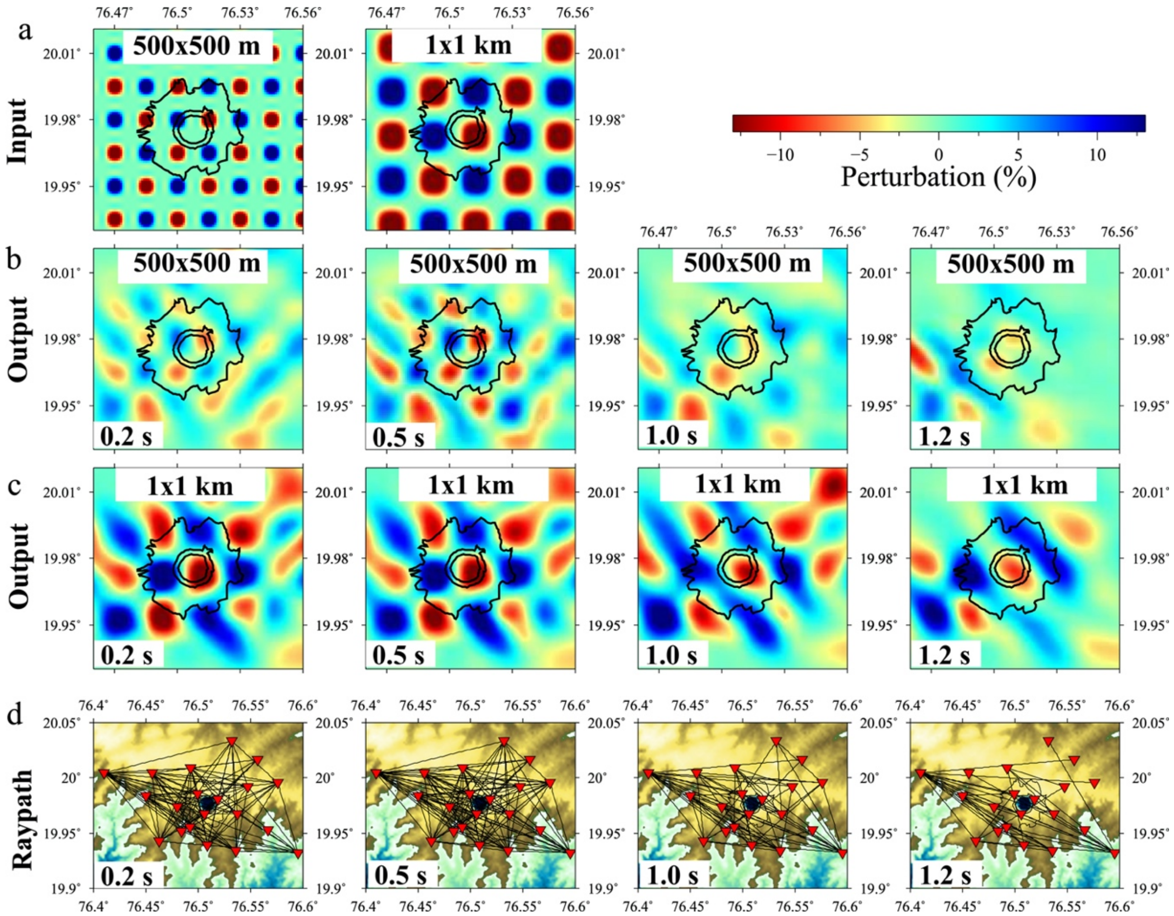

Figure 5: Sensitivity tests for spatial resolution. Two input checkerboard models of sizes equal to 500 m and 1 km are shown in (a) with their corresponding output models in (b) and (c) at different periods. Color data indicates perturbation from a mean velocity of 2 km/s. Corresponding raypath distributions are shown in (d).

We analyze the model resolution using a series of checkerboard tests considering positive and negative velocity anomalies of two different sizes, i.e., 500 x 500 m and 1 x 1 km, with a 1 km spacing between them (Fig. 5a). Considering that the group velocity perturbation around the crater is 10-15 %, as discussed below, we selected a maximum velocity perturbation of 13% from the mean velocity of 2 km/s for the checkerboard tests. The recovered checkerboard patterns at representative periods are presented in Figs. 5b and c. Several interesting observations can be made from the test results. First, for both input models, the checkerboard patterns inside and immediately outside the ejecta zone are reasonably well resolved at shorter periods (≤ 1 s). At longer periods (> 1 s), the recovery potential decreases away from the crater's center. Second, the amplitude of the recovered patterns decreases with decreasing anomaly size. Recovered amplitudes in the case of the 1 x 1 km input model are higher (Fig. 5c) than those in the 500 x 500 m input model (Fig. 5b).

Additionally, the recovered amplitude decreases as the period increases. Possible reasons for such distortion at longer periods (> 1 s) may include a lack of raypath coverage (Fig. 5d) and poor SNR.

The checkerboard results show diagonally elongated patterns, particularly at longer periods (> 1 s). Such lateral smearing may result from a regular pattern and close proximity of input anomalies (Rawlinson & Spakman 2016), i.e., the input model does not have oscillating positive to negative anomalies in the diagonal direction (Fig. 5a), and the anomalies are closely spaced. That is why we get elongated patterns in the recovered checkerboard results when the path coverage is diagonally dominant, as observed here at longer periods (> 1 s). To avoid such a situation, we next perform spike tests assuming a low-velocity anomaly of sizes 500 m and 1 km beneath the crater's center (Figs. S2 and S3). For the anomaly size of 500 m, the results at periods ≤ 1 s show no significant lateral smearing, and at least 50 % of the amplitude is recovered. For the 1 km-sized anomaly, we see no significant lateral smearing at all periods (up to 1.2 s), and the amplitude recovery varies from 60-100 %. These experiments show that our lateral resolution around the crater varies from 0.5 to 1 km for the period range (0.1 to 1.2 s) considered in this study. Given that the Lonar crater has a rim-to-rim diameter of ~1.8 km, this study's spatial resolution of 0.5-1 km is sufficient to image the crater's geometry.

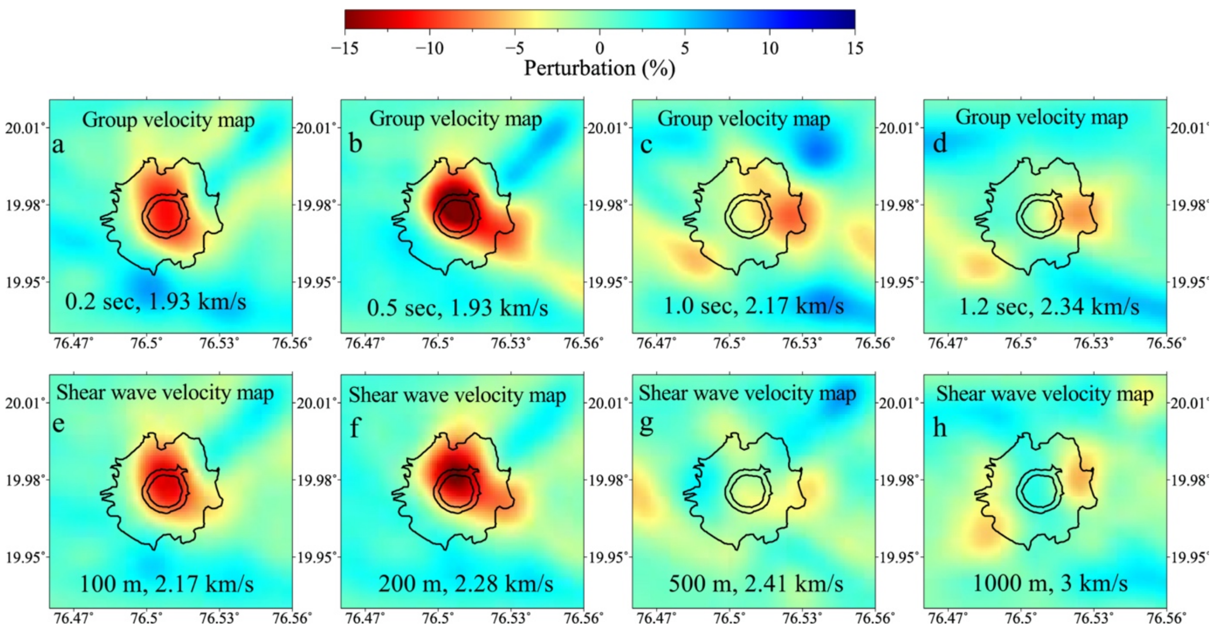

Figure 6: Group velocity maps (top panel) and shear wave velocity maps (bottom panel) as perturbation from regional mean are presented in (a-d) and (e-h), respectively.

Next, we perform group velocity tomography from 0.1 to 1.2 seconds at an interval of 0.1 seconds and generate group velocity maps at a grid interval of 0.005 x 0.005°. The group velocity maps at periods of 0.2, 0.5, 1.0, and 1.2 s are shown in Fig. 6(a-d). L-curve tests and travel-time residuals are presented in Figs. S4 and S5. A key observation from the group velocity maps is the emergence of a low-velocity zone below the impact crater at a short period (< 1 s) that fades at periods ≥ 1 s. Note that the group velocity at a given period represents the response of a depth average of velocities. In order to compute the shear wave velocity with depth, we invert the group velocity at a grid node following the approach discussed below.

3.3 Shear wave velocity model

The group velocities at each grid point from periods 0.1 to 1.2 s are inverted using an iterative least-square 1D inversion scheme of Hermann (2013). The depth of the investigation is based on the group velocity sensitivity curve, which suggests that for a 1.2 s period, as in the present study, the group velocity has peak sensitivity at a depth of 1 km and decreases by 50 % beyond 1.5 km (Fig. S6). The initial velocity model for the inversion is a stack of layered Earth up to 1.5 km depth lying over a half-space. Layers have a thickness of 100 m and a shear velocity of 3 km/s. The result of a least-squared inversion may be strongly dependent on the choice of initial model and damping parameter (Foti *et al*. 2018). It is often advised to repeat the inversion with differing initial models and damping parameters (e.g., Crosbie *et al*. 2019). Figure S7 shows details of the 1D inversion. First, we randomly perturb the initial velocity model by 10 % and create 100 starting models. To compute the optimum damping parameter, we performed the L-cure test (Fig. S7c), which suggested a value between 0.1 and 1. For each starting model (out of 100), we run the inversion for 10 damping parameters between 0.1 and 1.0, thereby generating a set of 1000 inverted models at a single grid point. The final velocity model and its uncertainties are computed from the mean and standard deviation of the set of 1000 models. This process is repeated at all grid points and ultimately interpolated to produce a 3D shear wave velocity model. Although we choose to perturb the initial model by 10 % only, test inversions with 5 % (Fig. S8) and 20 % (Fig. S9) perturbations produce similar results (Fig. S10). Additionally, we also tested the inversion scheme with a low damping (Fig. S11) and a high damping parameter (Fig. S12), which showed no significant change in the final models (Fig. S13). These experiments ensure that the final velocity model is least sensitive to the choice of the starting models and regularization parameters.

In Fig. 6(e-h), we present the shear wave velocity maps at depths of 100 m, 200 m, 500 m, and 1000 m as perturbations from the regional mean. At shallow depths (< 500 m), velocity beneath the crater is reduced by 10-15 % compared to regions outside the ejecta zone. At deeper depths, we don't observe any significant lateral variation in velocity, indicating the depth of influence of impact cratering is restricted to about 500 m. In the following section, we discuss the geometry of the impact crater using this velocity model.

4. Results and Discussion

The most common geophysical signature of simple impact craters is the observation of circular/semi-circular negative gravity anomaly, indicating density reduction due to fracturing and brecciation of the target rocks (Morgan *et al*. 2013; Pilkington & Grieve 1992). This is also reflected as a reduction in seismic velocities. Based on these signatures, the depth extent of the low-velocity breccia zone (i.e., true depth of the crater) is modelled in terms of the diameter (D) of simple craters as $d_t = 0.28\ D^{1.02}$, where d_t is the true depth (Grieve *et al*. 1989; Pilkington & Grieve 1992). This scaling relation for simple craters is generally accepted worldwide. However, ground-truthing of this relationship requires high-resolution imaging of simple craters and measurement of the depth extent of the low-velocity anomaly.

A review of the previous studies around the Lonar crater indicates that the true geometry of the crater is poorly known. The first attempt to image the crater's depth comes from five drill holes into the crater floor reaching up to 300-400 m depth below the floor level (Fredriksson *et al*. 1973; Fudali *et al*. 1980). Using the first three drill holes, Fredriksson *et al*. (1973) produced a depth cross-section showing a sedimentary layer with a maximum thickness of 100 m overlying a brecciated zone whose thickness exceeds 225 m. Later, Fudali *et al*. (1980) concluded that four of the five drill holes did not actually reach the true bottom of the crater. Additionally, no consistent core-to-core correlation from all five drill holes was obtained, indicating that the exact extent of the brecciated zone is unknown (Fudali *et al*. 1980; Kiik *et al*. 2020).

Modelling of gravity and magnetic data by Rajasekhar & Mishra (2005) showed a circular/semi-circular gravity low and a magnetic high anomaly at the center of the crater. The high magnetic anomaly was interpreted as dike-like bodies within the breccia zone having high magnetization due to magnetite that may represent parts of the meteorite. The crater's depth was modelled to be about 500-600 m below the surface. In contrast, Kiik *et al*. (2020) observed a negative magnetic anomaly over the crater and concluded that the post-impact brecciation and random distribution of clasts weaken the remanent magnetization compared to the surrounding Deccan basalts. Such a discrepancy in the magnetic model may arise from the complex nature of the breccia zone, which is largely unknown.

Seismic studies at the Lonar crater are very limited. Sivaram *et al*. (2018) used the same data as this study and provided a shear wave velocity model of the crater up to 600-750 m below the surface. They first computed the ambient noise horizontal-to-vertical spectral ratio (HVSR) in the frequency range of 0.2 to 20 Hz. Using ambient noise tomography, as used in the present study, the authors obtained surface wave dispersion in the frequency range of 0.2 to ~1 Hz. Because the observed surface wave data lacks high-frequency content (0.2 to 20 Hz), the authors first inverted the surface wave dispersion (0.2 to 1 Hz) to produce a shear wave velocity model. Sivaram *et al*. (2018) subsequently used this velocity model to theoretically compute surface wave dispersion data in the frequency range of 0.2-20 Hz and jointly invert it with the HVSR data. Evidently, their dispersion data in the high-frequency range (0.2-20 Hz) does not truly represent the subsurface geology. The final model is a shear wave velocity model up to 750 m depth at each station shown in Fig. 1b. The study fails to resolve the velocity reduction due to the post-impact modifications of the target rock, possibly due to a lack of high-frequency (> 1 Hz) surface waves required to image a shallow impact crater and insufficient lateral resolution. Note that the velocity model in Sivaram *et al*. (2018) is presented at each station with an average inter-station spacing of more than 2 km, which is inadequate to resolve the Lonar crater with a diameter of ~1.8 km. From these discussions, it is clear that the exact geometry of the Lonar crater is still sketchy. Our velocity model, presented in this study, has a lateral resolution of 0.5 to 1 km in the period range of 0.1 to 1.2 s, which is a significant improvement compared to any previous study in the region and has the required potential to resolve the Lonar crater.

Laboratory measurements of Vs in basalt below the Lonar crater are around 2.45 km/s (Lakshmi & Kumar 2020). This velocity measurement is performed at room conditions, and hence it indicates the upper limit. Drill holes in the Koyna-Warna region of the DVP, situated ~450 km west of the Lonar crater, provide in-situ velocity measurements up to 900 m depth (Ray *et al*. 2021). The basalt has a velocity increasing with depth from 1.44 to 2.44 km/s and is underlain by the basement rock with an average Vs of 2.55 km/s. In this discussion, we use the reference velocities for basalt and basement as 2.45 km/s and 2.55 km/s, respectively.

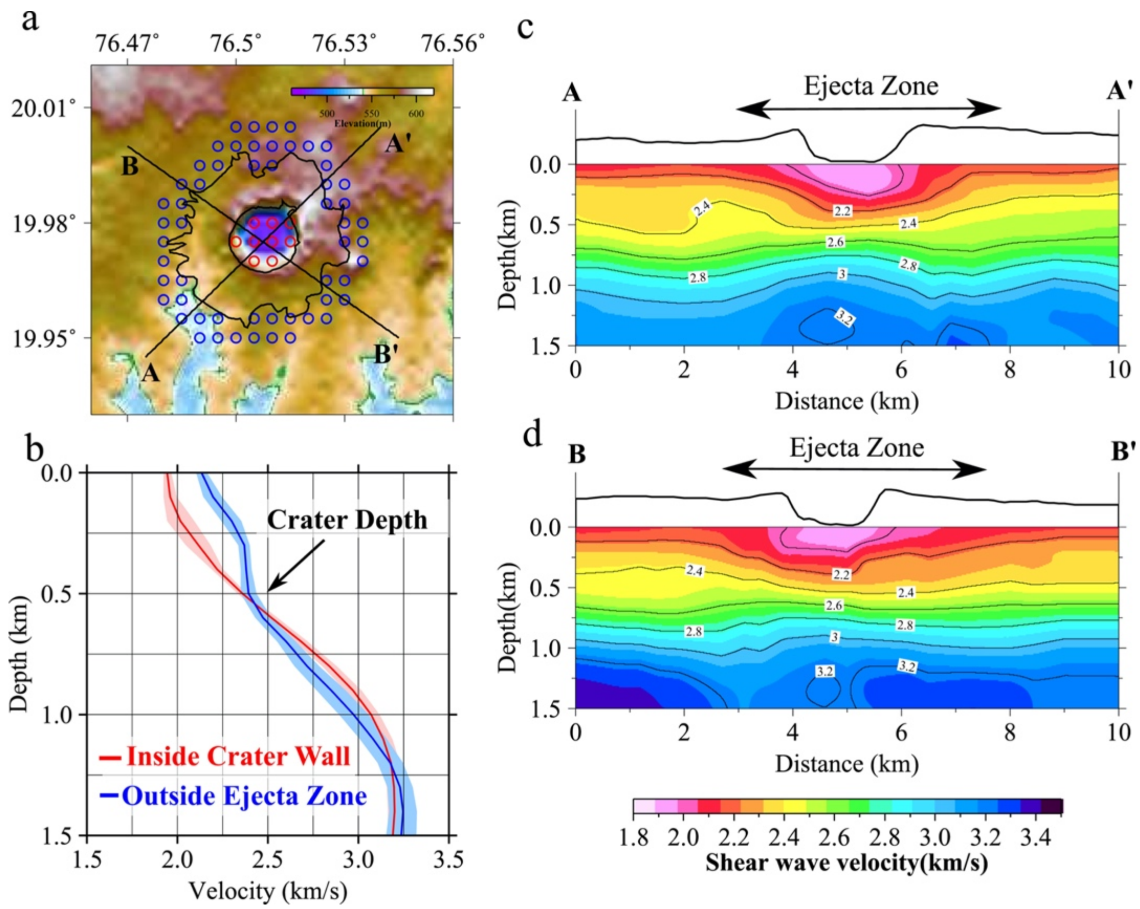

Figure 7: Shear wave velocity – depth structure across the Lonar lake. (a) locations of velocity profiles are marked as solid and straight black lines. Red dots indicate the inside of the crater, whereas blue dots represent the area outside the ejecta zone. (b) comparison of velocity models below the crater and away from it. The shaded regions indicate one standard deviation of the velocities from grid points in red and blue dots. Two velocity-depth profiles are shown in (c) and (d). The vertical axis is depth, and the horizontal axis is the distance from the left side of the profiles. The solid black line on top of the profiles indicates local topography. Solid black lines inside the velocity profiles are velocity contours.

The two velocity-depth profiles (Figs. 7c and d) crossing the crater show reduced shear wave velocity below the crater's rim: Vs < 2 km/s up to a depth of 250 m and 2-2.4 km/s from 250 m to ~500 m. Outside the ejecta zone, the velocity increases progressively from 2.15 km/s to 2.4 km/s in the top 250 m and is nearly constant (Vs ~ 2.4 km/s) for the next 250 m. Beyond 500 m depth, the Vs is more than 2.5 km/s both off and on the crater. Sivaram *et al*. (2018) observed a Vs < 1.5 km/s reaching up to 750 m depth around the crater, which is an underestimation of velocity values compared to the model presented in this study. The low velocity below the crater is bowl-shaped, typical for a simple crater (Pilkington & Grieve 1992). The areas outside the ejecta zone can be considered the pre-impact structure. A comparison between the velocity model below the lake's center and outside the ejecta zone is shown in Fig. 7b. Clearly, the depth extent of the low velocity is not more than 500 m. Furthermore, the mean velocity beneath the crater wall is slightly higher than outside the ejecta zone between a depth of 500 m and 1.2 km. However, the velocity values only differ by less than 2 % at depths beyond 500 m, possibly representing the local variation in the basement rocks. The Vs range below 250 m outside the ejecta zone is consistent with the laboratory-determined value of ~2.45 km/s (Lakshmi & Kumar 2020). The basalt thickness in the Lonar area can be mapped at ~500-600 m using the velocity constraint discussed above.

Table 1.

Study	**Estimated depth of the crater (m)**
Fredriksson et al., 1973	> 400 m (from drill hole data)
Pilkington & Grieve, 1992	509 m (from scaling relation)
Rajasekhar & Mishra (2005)	500-600 m (from gravity and magnetic data)
Sivaram et al. (2018)	> 600 m (from seismic data)
This study	500 m (from seismic data)

This study provides the first seismic velocity model that resolves the impact-induced low-velocity structure below the Lonar crater caused by the fracturing of target rocks and is consistent with the global geophysical response of impact craters (Pilkington & Grieve 1992). Furthermore, the study also provides ground truth for the scaling relationship of the crater's depth-diameter presented in Grieve *et al*. (1989). The depth extent of low velocity is ~500 m, representing the crater's true depth, and is consistent with the depth-diameter relation ($d_t = 0.28\ D^{1.02} = 509$ m for D=1.8 km). For comparison purposes, Table 1 provides a compilation of depth estimates from previous studies and this study. Although the depth estimates from previous studies vary considerably from 400 m to more than 600 m, our depth estimate of ~ 500 m shows a general consistency with previous results. The present study also highlights the effectiveness of ambient noise data in imaging the shallow impact craters and mapping sub-basalt targets on the Earth and other planets using recent deployments of seismographs.

5. Conclusions

Ambient noise analysis of 20 broadband seismic stations around the Lonar impact crater provides group velocity maps in the period range of 0.1 to 1.2 seconds with a lateral resolution of 0.5-1 km. The dominant noise source is cultural, possibly generated by the traffic on the state highways. We invert the group velocity data for shear wave velocity variation with the depth of the Lonar crater up to a depth of 1.5 km. Key findings of the study are presented in Fig. 7 and listed below:

1. The impact crater is characterized by a low-velocity zone, where Vs is reduced by 10-15 % compared to regions outside the ejecta zone.
2. The depth extent of the low-velocity zone, which is estimated to be 500 m below the crater's center, corresponds to the crater's true depth.
3. The estimated true depth of the crater in this study is consistent with the depth-diameter scaling relation of global simple craters.

6. Acknowledgements

This work was supported by the Department of Atomic Energy grant in the form of a Research Associateship to VK and Raja Ramanna Fellowship to SSR. SSR acknowledges the support of his colleagues K. Sivaram, Gokul Saha, BNV Prasad, Sudesh Kumar, and Somasish Bose of the CSIR-National Geophysical Research Institute, Hyderabad, for their help in acquiring seismological data used in this study. The field experiment from March to December 2014 was supported by the JC Bose fellowship grant of the Ministry of Science and Technology to SSR. Critical comments from Christian Stanciu and an anonymous reviewer helped improve the manuscript. The authors also thank editor Andrea Morelli. All figures were prepared using the Generic Mapping Tool (GMT) developed by Wessel et al. (2013).

7. Data Availability Statement

Seismic waveform of the ambient noise cross-correlations, the group velocity and the 3D shear wave velocity at each grid-node are included in the supplementary data.

8. References

Acevedo, J., Fernández-Viejo, G., Llana-Fúnez, S., López-Fernández, C. and Olona, J., 2019. Ambient noise tomography of the southern sector of the Cantabrian Mountains, NW Spain. *Geophysical Journal International*, *219*(1), pp.479-495. https://doi.org/10.1093/gji/ggz308

Ahrens, T.J., Xia, K. and Coker, D., 2002, July. Depth of cracking beneath impact craters: New constraint for impact velocity. In *AIP Conference Proceedings* (Vol. 620, No. 1, pp. 1393-1396). American Institute of Physics. https://doi.org/10.1063/1.1483799

Barton, P.J., Grieve, R.A.F., Morgan, J.V., Surendra, A.T., Vermeesch, P.M., Christeson, G.L., Gulick, S.P.S. and Warner, M.R., 2010. Seismic images of Chicxulub impact melt sheet and comparison with the Sudbury structure. https://doi.org/10.1130/2010.2465(07)

Bell, C., Morgan, J.V., Hampson, G.J. and Trudgill, B., 2004. Stratigraphic and sedimentological observations from seismic data across the Chicxulub impact basin. *Meteoritics & Planetary Science*, *39*(7), pp.1089-1098. https://doi.org/10.1111/j.1945-5100.2004.tb01130.x

Bensen, G.D., Ritzwoller, M.H., Barmin, M.P., Levshin, A.L., Lin, F., Moschetti, M.P., Shapiro, N.M. and Yang, Y., 2007. Processing seismic ambient noise data to obtain reliable broad-band surface wave dispersion measurements. *Geophysical journal international*, *169*(3), pp.1239-1260. https://doi.org/10.1111/j.1365-246X.2007.03374.x

Chen, G., Cheng, Q., Luo, Y., Yang, Y., Xu, H. and Deng, X., 2021. Seismic imaging of the Caosiyao giant porphyry molybdenum deposit using ambient noise tomography. *Geophysics*, *86*(6), pp.B401-B412. https://doi.org/10.1190/geo2021-0117.1

Christeson, G.L., Nakamura, Y., Buffler, R.T., Morgan, J. and Warner, M., 2001. Deep crustal structure of the Chicxulub impact crater. *Journal of Geophysical Research: Solid Earth*, *106*(B10), pp.21751-21769. https://doi.org/10.1029/2001JB000337

Collins, G.S., Melosh, H.J. and Marcus, R.A., 2005. Earth impact effects program: A web-based computer program for calculating the regional environmental consequences of a meteoroid impact on Earth. *Meteoritics & planetary science*, *40*(6), pp.817-840. https://doi.org/10.1111/j.1945-5100.2005.tb00157.x

Collins, G.S., Melosh, H.J. and Osinski, G.R., 2012. The impact-cratering process. *Elements*, *8*(1), pp.25-30. https://doi.org/10.2113/gselements.8.1.25

Colombi, A., Chaput, J., Brenguier, F., Hillers, G., Roux, P. and Campillo, M., 2014. On the temporal stability of the coda of ambient noise correlations. *Comptes Rendus Geoscience*, *346*(11-12), pp.307-316. https://doi.org/10.1016/j.crte.2014.10.002

Crosbie, K.J., Abers, G.A., Mann, M.E., Janiszewski, H.A., Creager, K.C., Ulberg, C.W. and Moran, S.C., 2019. Shear velocity structure from ambient noise and teleseismic surface wave tomography in the cascades around Mount St. Helens. *Journal of Geophysical Research: Solid Earth*, *124*(8), pp.8358-8375. https://doi.org/10.1029/2019JB017836

Dziewonski, A., Bloch, S. and Landisman, M., 1969. A technique for the analysis of transient seismic signals. *Bulletin of the seismological Society of America*, *59*(1), pp.427-444. https://doi.org/10.1785/BSSA0590010427

Fichtner, A., 2015. Source-structure trade-offs in ambient noise correlations. *Geophysical Journal International*, *202*(1), pp.678-694. https://doi.org/10.1093/gji/ggv182

Foti, S., Hollender, F., Garofalo, F., Albarello, D., Asten, M., Bard, P.Y., Comina, C., Cornou, C., Cox, B., Di Giulio, G. and Forbriger, T., 2018. Guidelines for the good practice of surface wave analysis: a product of the InterPACIFIC project. *Bulletin of Earthquake Engineering*, *16*, pp.2367-2420. https://doi.org/10.1007/s10518-017-0206-7

Froment, B., Campillo, M., Roux, P., Gouedard, P., Verdel, A. and Weaver, R.L., 2010. Estimation of the effect of nonisotropically distributed energy on the apparent arrival time in correlations. *Geophysics*, *75*(5), pp.SA85-SA93. https://doi.org/10.1190/1.3483102

Fredriksson, K., Dube, A., Milton, D.J. and Balasundaram, M.S., 1973. Lonar Lake, India: An impact crater in basalt. *Science*, *180*(4088), pp.862-864. DOI: 10.1126/science.180.4088.862

Fudali, R.F., Milton, D.J., Fredriksson, K. and Dube, A., 1980. Morphology of Lonar crater, India: comparisons and implications. *The Moon and the Planets*, *23*(4), pp.493-515. https://doi.org/10.1007/BF00897591

Grieve, R.A.F., Garvin, J.B., Coderre, J.M. and Rupert, J., 1989. Test of a geometric model for the modification stage of simple impact crater development. *Meteoritics*, *24*(2), pp.83-88. https://doi.org/10.1111/j.1945-5100.1989.tb00948.x

Gulick, S.P.S., Christeson, G.L., Barton, P.J., Grieve, R.A.F., Morgan, J.V. and Urrutia-Fucugauchi, J., 2013. Geophysical characterization of the Chicxulub impact crater. *Reviews of Geophysics*, *51*(1), pp.31-52. https://doi.org/10.1002/rog.20007

Gulick, S.P., Barton, P.J., Christeson, G.L., Morgan, J.V., McDonald, M., Mendoza-Cervantes, K., Pearson, Z.F., Surendra, A., Urrutia-Fucugauchi, J., Vermeesch, P.M. and Warner, M.R., 2008. Importance of pre-impact crustal structure for the asymmetry of the Chicxulub impact crater. *Nature Geoscience*, *1*(2), pp.131-135. https://doi.org/10.1038/ngeo103

Hanafy, S.M., Soupios, P., Stampolidis, A., Koch, C.B., Al-Ramadan, K., Al-Shuhail, A., Solling, T. and Argadestya, I., 2021. Comprehensive Geophysical Study at Wabar Crater, Rub Al-Khali Desert, Saudi Arabia. *Earth and Space Science*, *8*(9), p.e2020EA001432. https://doi.org/10.1029/2020EA001432

Harinarayana, T., Patro, B.P.K., Veeraswamy, K., Manoj, C., Naganjaneyulu, K., Murthy, D.N. and Virupakshi, G., 2007. Regional geoelectric structure beneath Deccan Volcanic Province of the Indian subcontinent using magnetotellurics *Tectonophysics*, *445*(1-2), pp.66-80. https://doi.org/10.1016/j.tecto.2007.06.010

Herrmann, R.B., 2013. Computer programs in seismology: An evolving tool for instruction and research. *Seismological Research Letters*, *84*(6), pp.1081-1088. https://doi.org/10.1785/0220110096

Jaxybulatov, K., Shapiro, N.M., Koulakov, I., Mordret, A., Landès, M. and Sens-Schönfelder, C., 2014. A large magmatic sill complex beneath the Toba caldera. *science*, *346*(6209), pp.617-619. http://doi.org/10.1126/science.1258582

Johnson, C.W., Meng, H., Vernon, F. and Ben-Zion, Y., 2019. Characteristics of ground motion generated by wind interaction with trees, structures, and other surface obstacles. *Journal of Geophysical Research: Solid Earth*, *124*(8), pp.8519-8539. https://doi.org/10.1029/2018JB017151

Jourdan, F., Moynier, F., Koeberl, C. and Eroglu, S., 2011. 40Ar/39Ar age of the Lonar crater and consequence for the geochronology of planetary impacts. *Geology*, *39*(7), pp.671-674. https://doi.org/10.1130/G31888.1

Kenkmann, T., Poelchau, M.H. and Wulf, G., 2014. Structural geology of impact craters. *Journal of Structural Geology*, *62*, pp.156-182. https://doi.org/10.1016/j.jsg.2014.01.015

Kiik, K., Plado, J., Lingadevaru, M., Jeelani, S.H. and Szyszka, M., 2020. Magnetic Anomaly and Model of the Lonar Meteorite Impact Crater in Maharashtra, India. *Geosciences*, *10*(10), p.417. https://doi.org/10.3390/geosciences10100417

Krishnamurthy, P., 2020. The Deccan volcanic province (DVP), India: a review. *Journal of the Geological Society of India*, *96*(1), pp.9-35. https://doi.org/10.1007/s12594-020-1501-5

Kumar, P.S., 2005. Structural effects of meteorite impact on basalt: Evidence from Lonar crater, India. *Journal of Geophysical Research: Solid Earth*, *110*(B12). https://doi.org/10.1029/2005JB003662

Kumar, P.S., Prasanna Lakshmi, K.J., Krishna, N., Menon, R., Sruthi, U., Keerthi, V., Senthil Kumar, A., Mysaiah, D., Seshunarayana, T. and Sen, M.K., 2014. Impact fragmentation of Lonar Crater, India: Implications for impact cratering processes in basalt. *Journal of Geophysical Research: Planets*, *119*(9), pp.2029-2059. https://doi.org/10.1002/2013JE004543

Kumar, V., Rai, S.S., Hawkins, R. and Bodin, T., 2022. Seismic Imaging of Crust Beneath the Western Tibet-Pamir and Western Himalaya Using Ambient Noise and

Earthquake Data. *Journal of Geophysical Research: Solid Earth*, *127*(6), p.e2021JB022574. https://doi.org/10.1029/2021JB022574

La Touche, T.H.D. and Christie, W.A.K., 1912. The geology of the Lonar Lake. *Rec. Geol. Survey India*, *14*, pp.266-289.

Lakshmi, K.J.P. and Kumar, P.S., 2020. Physical properties of basalt ejecta boulders at Lonar crater, India: Insights into the target heterogeneity and impact spallation processes in basalt with application to Mars. *Journal of Geophysical Research: Planets*, *125*(10), p.e2020JE006593. https://doi.org/10.1029/2020JE006593

Li, X., Huang, J. and Liu, Z., 2020. Ambient-noise tomography of the Baiyun gold deposit in Liaoning, China. *Seismological Research Letters*, *91*(5), pp.2791-2802. https://doi.org/10.1785/0220190393

Liu, X., 2020. Finite-frequency sensitivity kernels for seismic noise interferometry based on differential time measurements. *Journal of Geophysical Research: Solid Earth*, *125*(4), p.e2019JB018932. https://doi.org/10.1029/2019JB018932

Lobkis, O.I. and Weaver, R.L., 2001. On the emergence of the Green's function in the correlations of a diffuse field. *The Journal of the Acoustical Society of America*, *110*(6), pp.3011-3017. https://doi.org/10.1121/1.1417528

Maloof, A.C., Stewart, S.T., Weiss, B.P., Soule, S.A., Swanson-Hysell, N.L., Louzada, K.L., Garrick-Bethell, I. and Poussart, P.M., 2010. Geology of lonar crater, India. *Bulletin*, *122*(1-2), pp.109-126. https://doi.org/10.1130/B26474.1

McNamara, D.E. and Boaz, R.I., 2006. *Seismic noise analysis system using power spectral density probability density functions: A stand-alone software package*. Reston, Virginia: US Geological Survey.

McNamara, D.E. and Buland, R.P., 2004. Ambient noise levels in the continental United States. *Bulletin of the seismological society of America*, *94*(4), pp.1517-1527. https://doi.org/10.1785/012003001

Melosh, H.J., 1989. Impact cratering: A geologic process. *New York: Oxford University Press; Oxford: Clarendon Press*.

Morgan, W.J., 1972. Deep mantle convection plumes and plate motions. *AAPG bulletin*, *56*(2), pp.203-213. https://doi.org/10.1306/819A3E50-16C5-11D7-8645000102C1865D

Morgan, J., Rebolledo-Vieyra, M., Osinski, G.R. and Pierazzo, E., 2013. Geophysical studies of impact craters. *Impact cratering processes and products*, pp.211-22. https://doi.org/10.1002/9781118447307

Osinski, G.R., Tornabene, L.L. and Grieve, R.A., 2011. Impact ejecta emplacement on terrestrial planets. *Earth and Planetary Science Letters*, *310*(3-4), pp.167-181. https://doi.org/10.1016/j.epsl.2011.08.012

Pierazzo, E. and Melosh, H.J., 2000. Understanding oblique impacts from experiments, observations, and modeling. https://doi.org/10.1146/annurev.earth.28.1.141

Pilkington, M. and Grieve, R.A.F., 1992. The geophysical signature of terrestrial impact craters. *Reviews of Geophysics*, *30*(2), pp.161-181. https://doi.org/10.1029/92RG00192

Preiswerk, L.E. and Walter, F., 2018. High-Frequency (> 2 Hz) Ambient Seismic Noise on High-Melt Glaciers: Green's Function Estimation and Source Characterization. *Journal of Geophysical Research: Earth Surface*, *123*(8), pp.1667-1681. https://doi.org/10.1029/2017JF004498

Rajasekhar, R.P. and Mishra, D.C., 2005. Analysis of gravity and magnetic anomalies over Lonar lake, India: An impact crater in a basalt province. *Current Science*, pp.1836-1840. https://www.jstor.org/stable/24110376

Rawlinson, N., 2005. FMST: fast marching surface tomography package–Instructions. *Research School of Earth Sciences, Australian National University, Canberra*, *29*, p.47. https://doi.org/10.1071/EG05341

Rawlinson, N. and Sambridge, M., 2005. The fast marching method: an effective tool for tomographic imaging and tracking multiple phases in complex layered media. *Exploration Geophysics*, *36*(4), pp.341-350. https://doi.org/10.1071/EG05341

Rawlinson, N. and Spakman, W., 2016. On the use of sensitivity tests in seismic tomography. *Geophysical Journal International*, *205*(2), pp.1221-1243. https://doi.org/10.1093/gji/ggw084

Ray, L., Gupta, R.K., Chopra, N., Gopinadh, D. and Dwivedi, S.K., 2021. Thermal and physical properties of Deccan basalt and Neoarchean basement cores from a deep scientific borehole in the Koyna− Warna seismogenic region, Deccan Volcanic Province, western India: Implications on thermal modeling and seismogenesis. *Earth and Space Science*, *8*(10), p.e2021EA001645. https://doi.org/10.1029/2021EA001645

Robbins, S.J., Watters, W.A., Chappelow, J.E., Bray, V.J., Daubar, I.J., Craddock, R.A., Beyer, R.A., Landis, M., Ostrach, L.R., Tornabene, L. and Riggs, J.D., 2018. Measuring impact crater depth throughout the solar system. *Meteoritics & Planetary Science*, *53*(4), pp.583-637. https://doi.org/10.1111/maps.12956

Sabra, K.G., Gerstoft, P., Roux, P., Kuperman, W.A. and Fehler, M.C., 2005. Surface wave tomography from microseisms in Southern California. *Geophysical Research Letters*, *32*(14). https://doi.org/10.1029/2005GL023155

Sager, K., Ermert, L., Boehm, C. and Fichtner, A., 2018. Towards full waveform ambient noise inversion. *Geophysical Journal International*, *212*(1), pp.566-590. https://doi.org/10.1093/gji/ggx429

Schimmel, M., Stutzmann, E. and Gallart, J., 2011. Using instantaneous phase coherence for signal extraction from ambient noise data at a local to a global scale. *Geophysical Journal International*, *184*(1), pp.494-506. https://doi.org/10.1111/j.1365-246X.2010.04861.x

Shapiro, N.M., Campillo, M., Stehly, L. and Ritzwoller, M.H., 2005. High-resolution surface-wave tomography from ambient seismic noise. *Science*, *307*(5715), pp.1615-1618. https://doi.org/10.1126/science.1108339

Sivaram, K., Gupta, S., Kumar, S. and Prasad, B.N.V., 2018. Shear velocity structural characterization around the Lonar crater using joint inversion of ambient noise HVSR and Rayleigh wave dispersion. *Journal of Applied Geophysics*, *159*, pp.773-784. https://doi.org/10.1016/j.jappgeo.2018.10.022

Tsai, V.C., 2009. On establishing the accuracy of noise tomography travel-time measurements in a realistic medium. *Geophysical Journal International*, *178*(3), pp.1555-1564. https://doi.org/10.1111/j.1365-246X.2009.04239.x

Weaver, R., Froment, B. and Campillo, M., 2009. On the correlation of non-isotropically distributed ballistic scalar diffuse waves. *The Journal of the Acoustical Society of America*, *126*(4), pp.1817-1826. https://doi.org/10.1121/1.3203359

Wessel, P., Smith, W.H., Scharroo, R., Luis, J. and Wobbe, F., 2013. Generic mapping tools: improved version released. *Eos, Transactions American Geophysical Union*, *94*(45), pp.409-410. https://doi.org/10.1002/2013EO450001

Yang, Y. and Ritzwoller, M.H., 2008. Characteristics of ambient seismic noise as a source for surface wave tomography. *Geochemistry, Geophysics, Geosystems*, *9*(2). https://doi.org/10.1029/2007GC001814

Yao, H. and Van Der Hilst, R.D., 2009. Analysis of ambient noise energy distribution and phase velocity bias in ambient noise tomography, with application to SE Tibet. *Geophysical Journal International*, *179*(2), pp.1113-1132. https://doi.org/10.1111/j.1365-246X.2009.04329.x

Supporting Information for

3D geometry of the Lonar impact crater, India, imaged from cultural seismic noise

Vivek Kumar[1], Shyam S. Rai[1]

[1]Department of Earth and Climate Science, Indian Institute of Science Education & Research Pune, Dr. Homi Bhabha Road, Pune 411008, India

Contents of this file

Figures S1 to S13

Table S1

Additional Supporting Information (Files uploaded separately)

1. Dataset S1: Seismic waveform of ambient noise cross-correlations, group velocity at each grid node, and inverted shear wave velocity.

Introduction

This supplementary document provides additional information on ambient noise data, resolution tests for the tomography, and the shear velocity model.

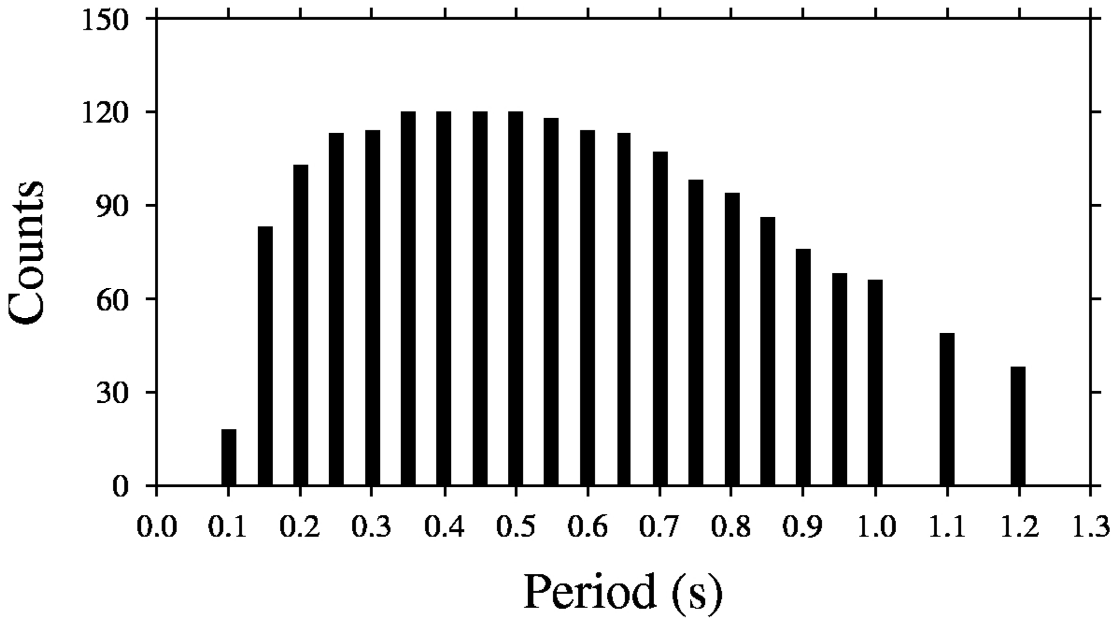

Figure S1. Number of ray paths in the period range of 0.1-1.2 s satisfying SNR > 5 and inter-station distance > one wavelength.

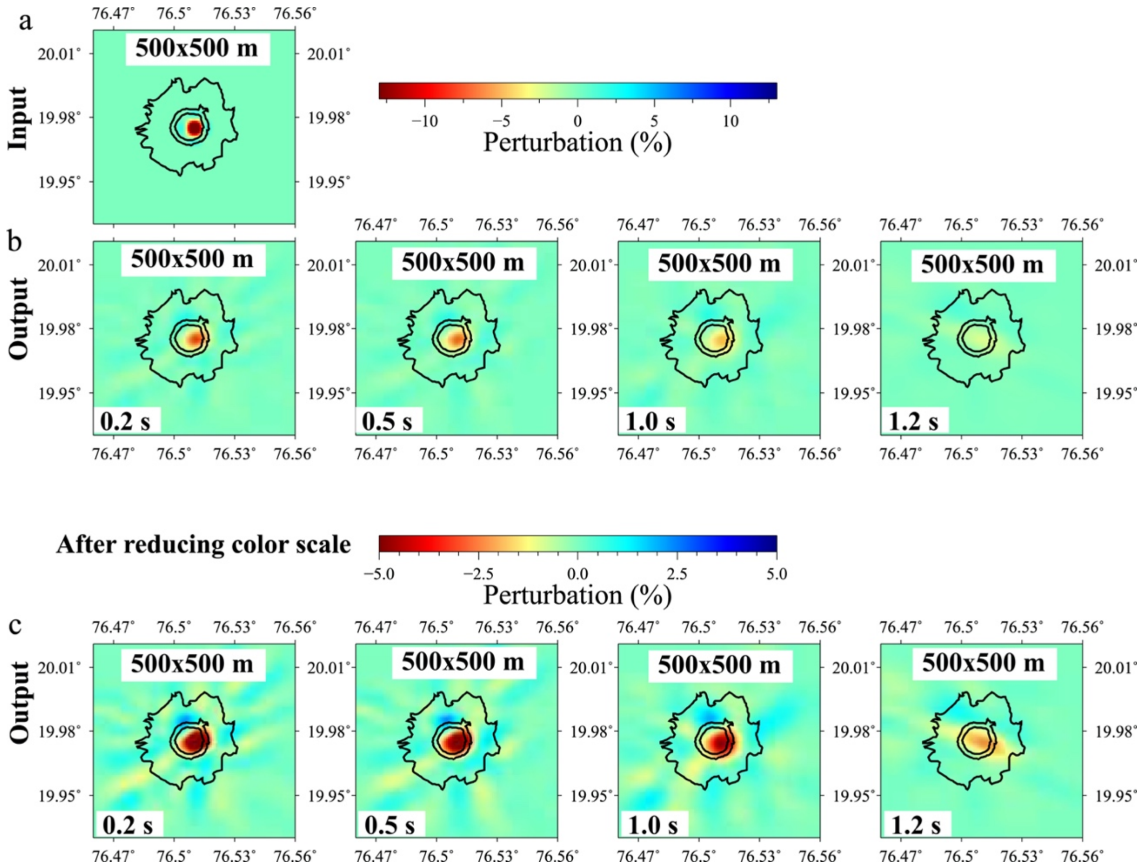

Figure S2. Spike test. An input low-velocity anomaly beneath the crater of size equal to 500 m is shown in (a) with its corresponding output models in (b). (c) represents the output models after reducing the limit on the color scale. Color data indicate perturbation from a mean velocity of 2 km/s.

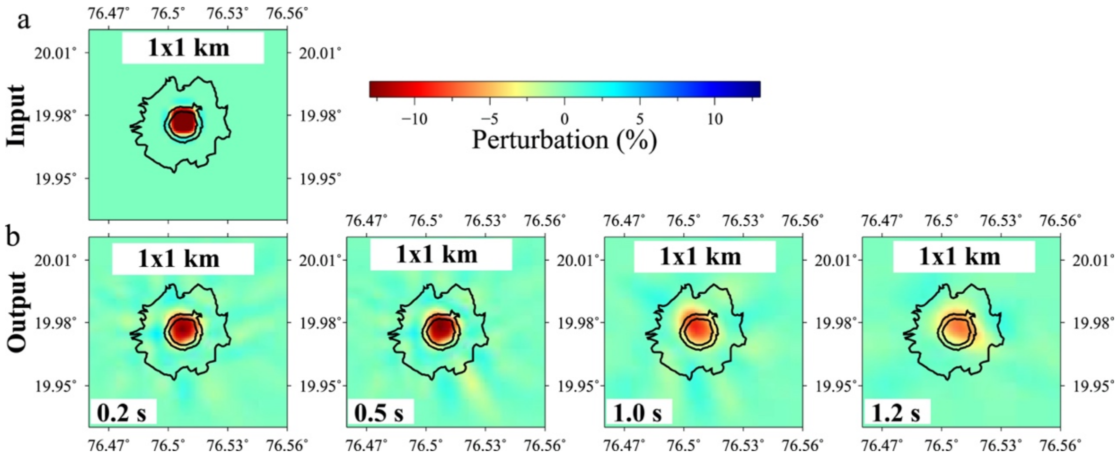

Figure S3. Spike test. An input low-velocity anomaly beneath the crater of size equal to 1 km is shown in (a) with its corresponding output models in (b). Color data indicate perturbation from a mean velocity of 2 km/s.

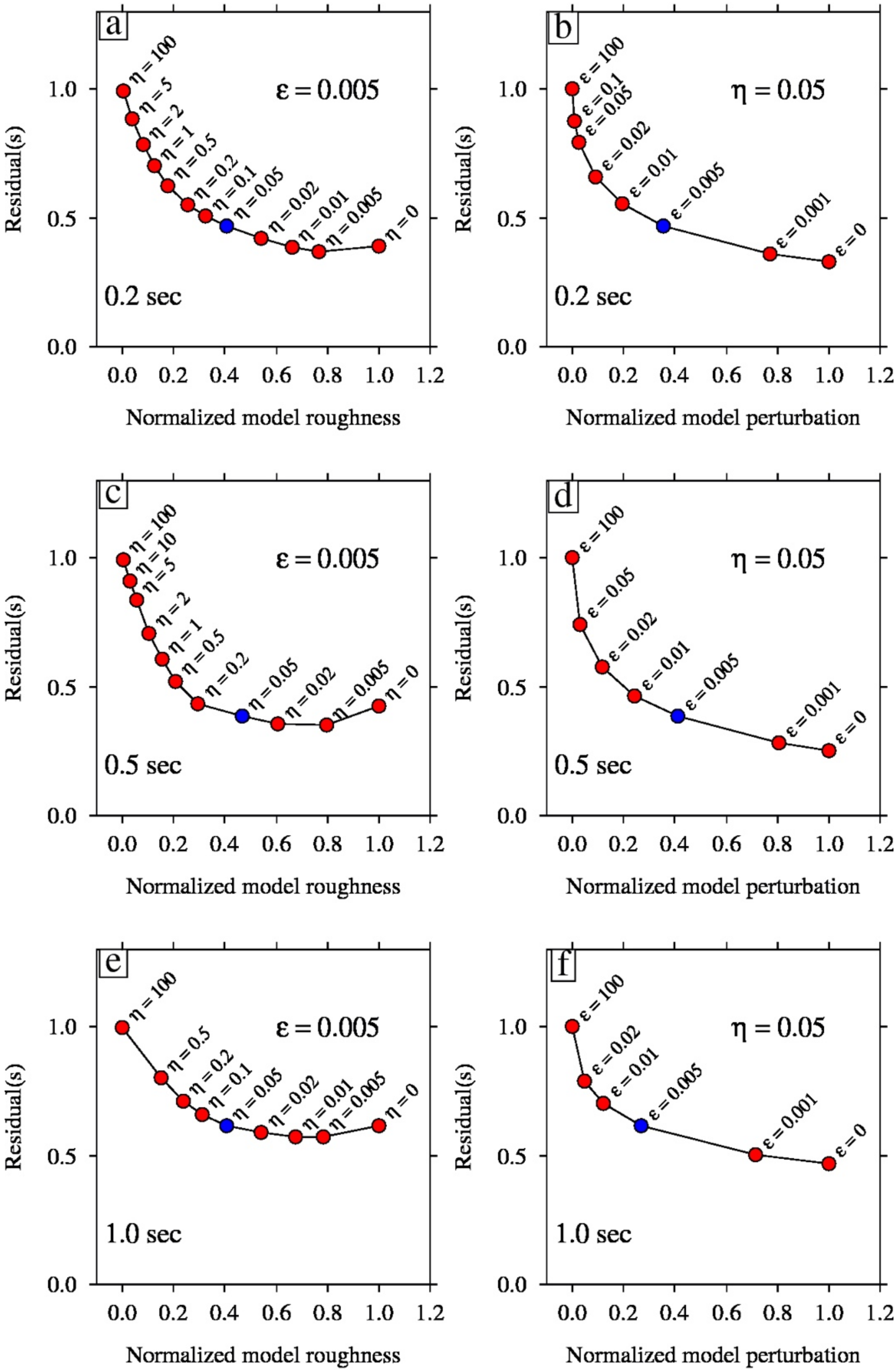

Figure S4. L-curve tests to determine regularization parameters at different periods. The left panel is for the smoothing parameter, and the right panel is for the damping parameter. The blue dot is the optimum regularization parameter.

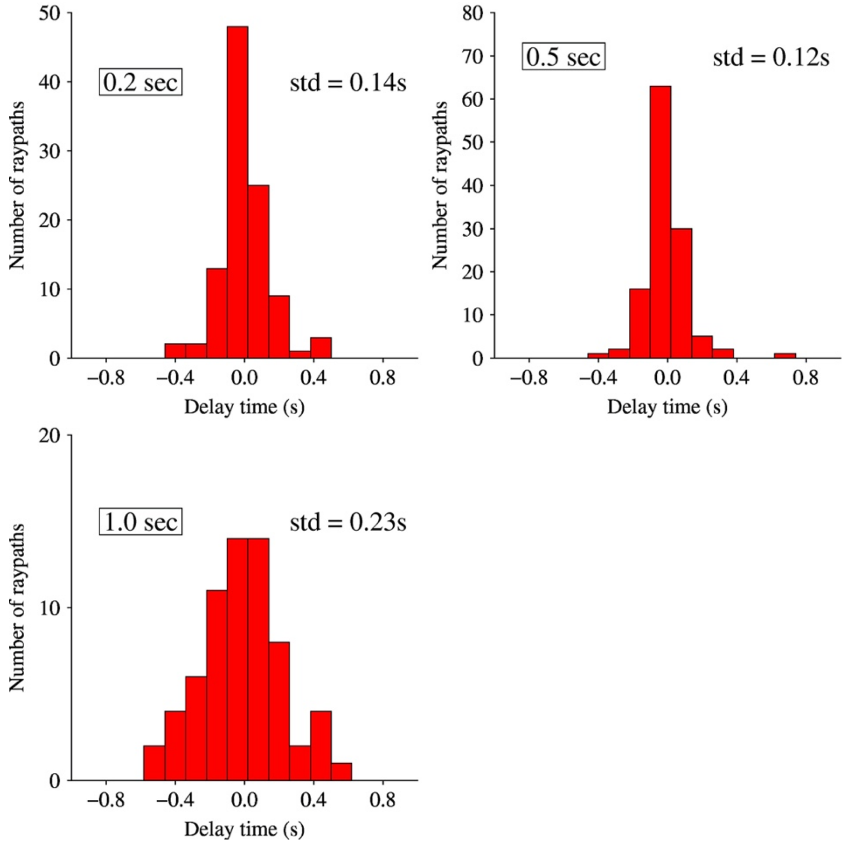

Figure S5. Travel-time residuals in group velocity tomography at different periods.

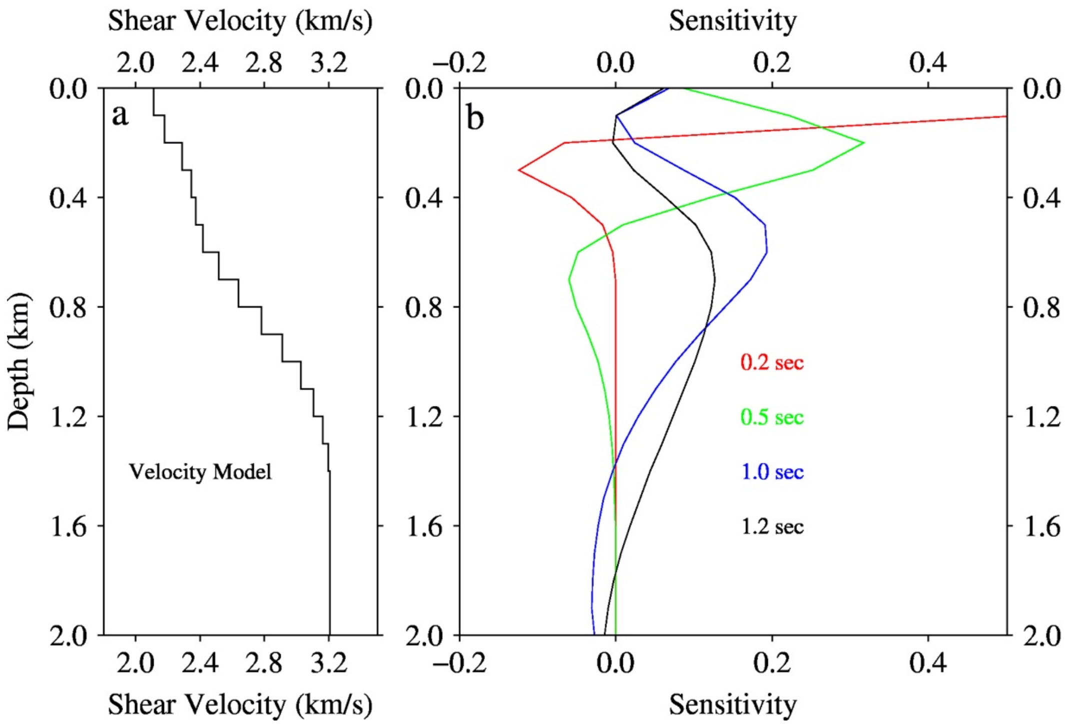

Figure S6. Group velocity sensitivity curve. (a) A reference velocity model, (b) sensitivity curve.

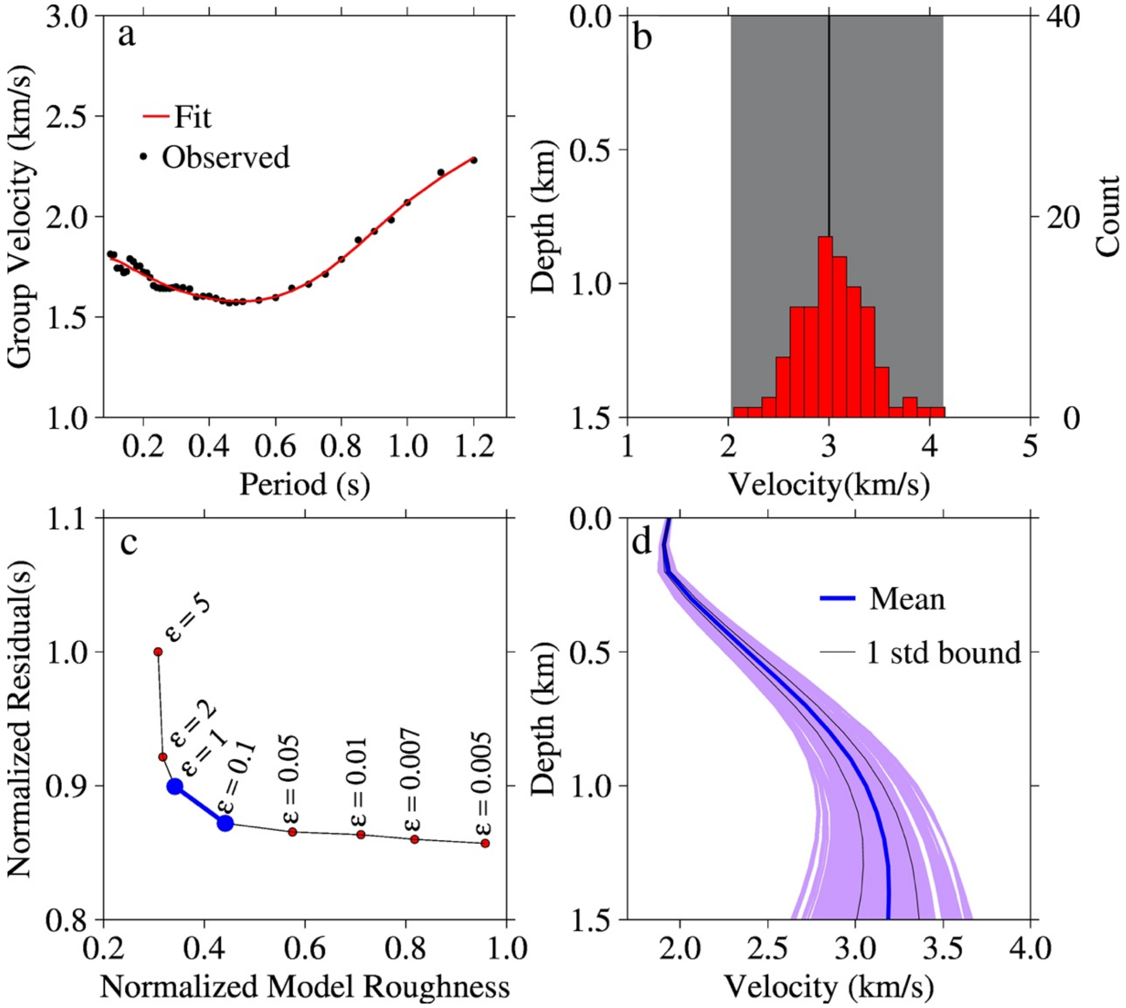

Figure S7. A sample 1D inversion showing repeated inversions with different initial models and damping parameters. (a) observed group velocity data at a grid point is shown as black dots, and a best fit is shown in solid red line after the inversion. (b) initial velocity model at 3 km/s is perturbed by 10% randomly to generate 100 initial models. The grey region shows the limit of the perturbation. The red histogram shows the distribution of perturbed models. (c) L-curve test for damping parameters. Optimum values lie between 0.1 and 1. We take 10 damping values between 0.1 and 1 and perform the inversion for each starting model. (d) Mean and standard deviation of models are shown in blue and black lines, respectively. The purple shade indicates all models.

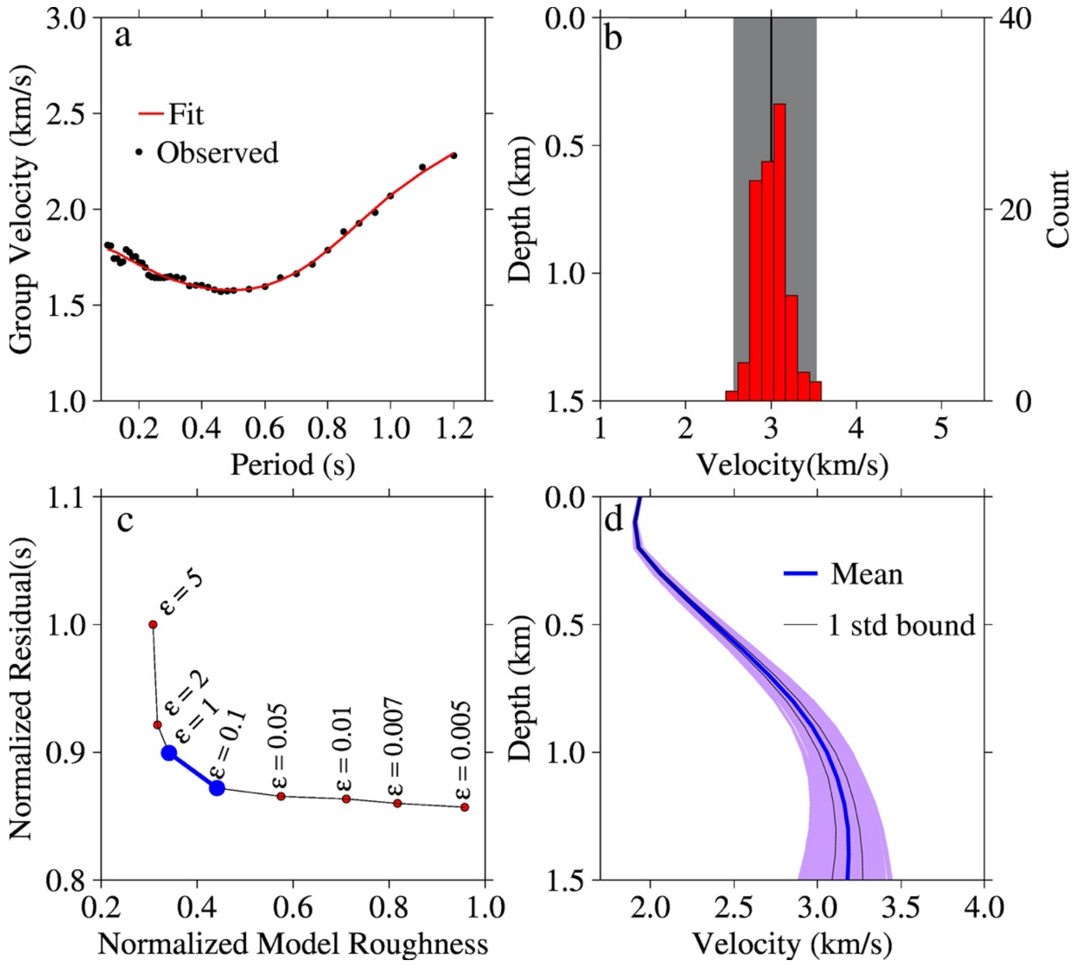

Figure S8. Same as Figure S7. The initial model is perturbed by 5 % only as shown in (b).

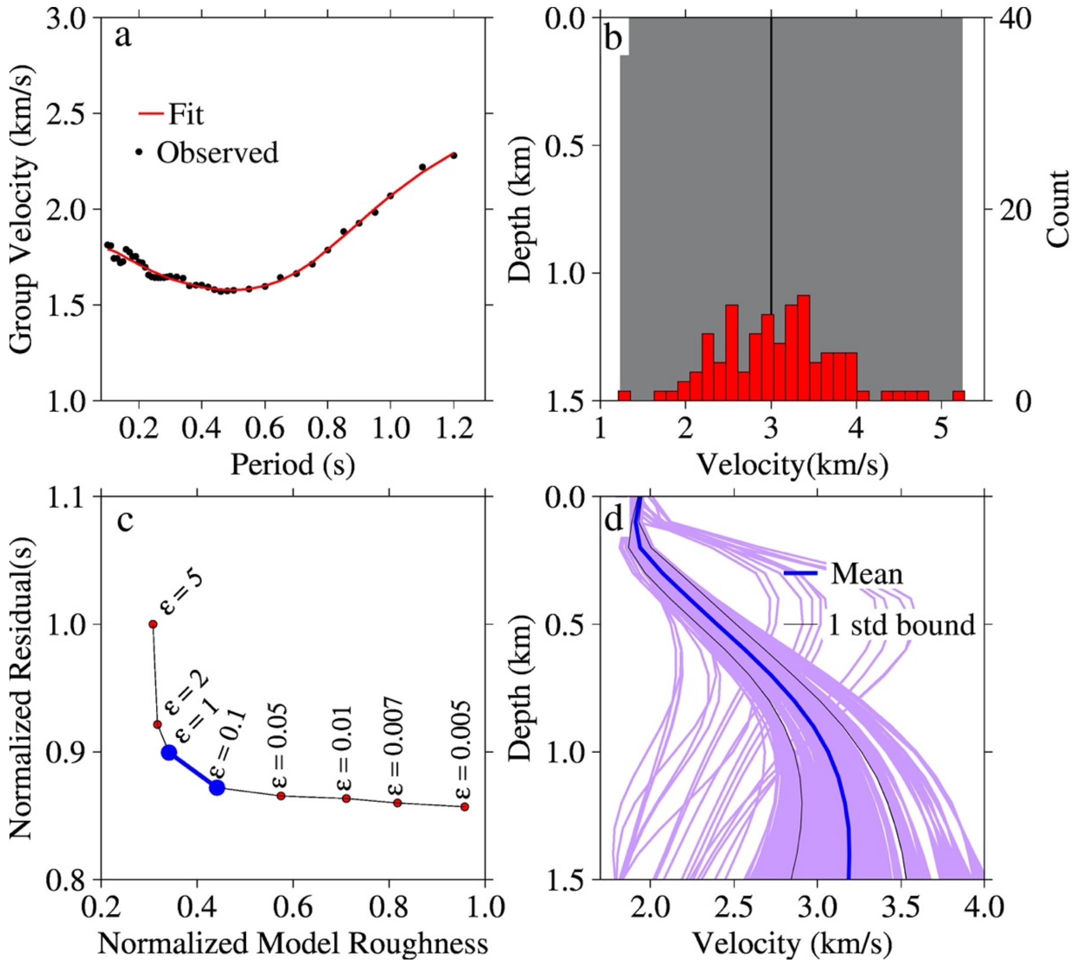

Figure S9. Same as Figure S7. The initial model is perturbed by 20 % only as shown in (b).

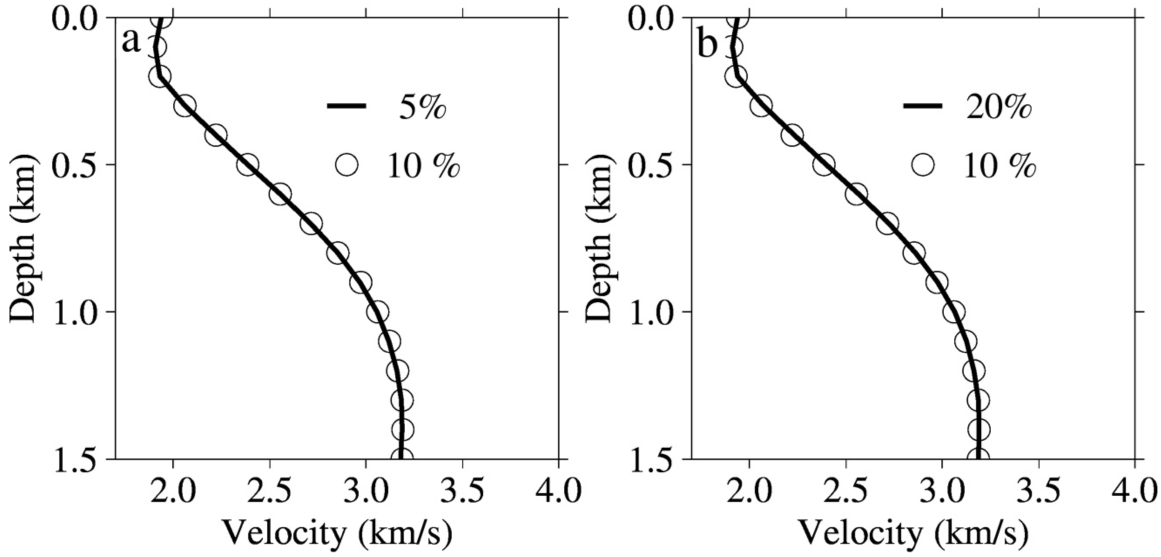

Figure S10. Comparison of mean velocity model obtained at 10% perturbation of initial model, as shown in Figure S7, with that obtained at (a) 5 % perturbation and (b) 20 % perturbation.

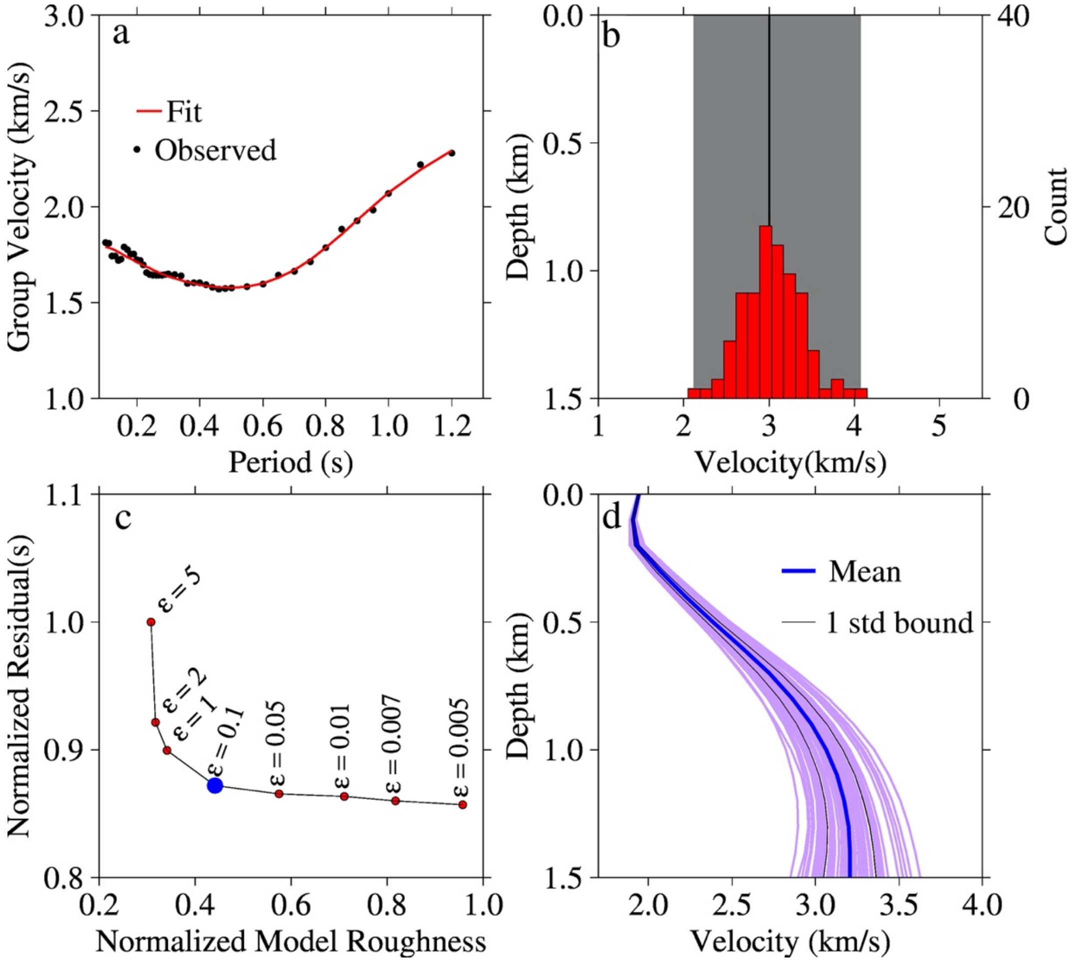

Figure S11. Same as Figure S7. The inversion is performed with a low damping value of 0.1 as shown in (c).

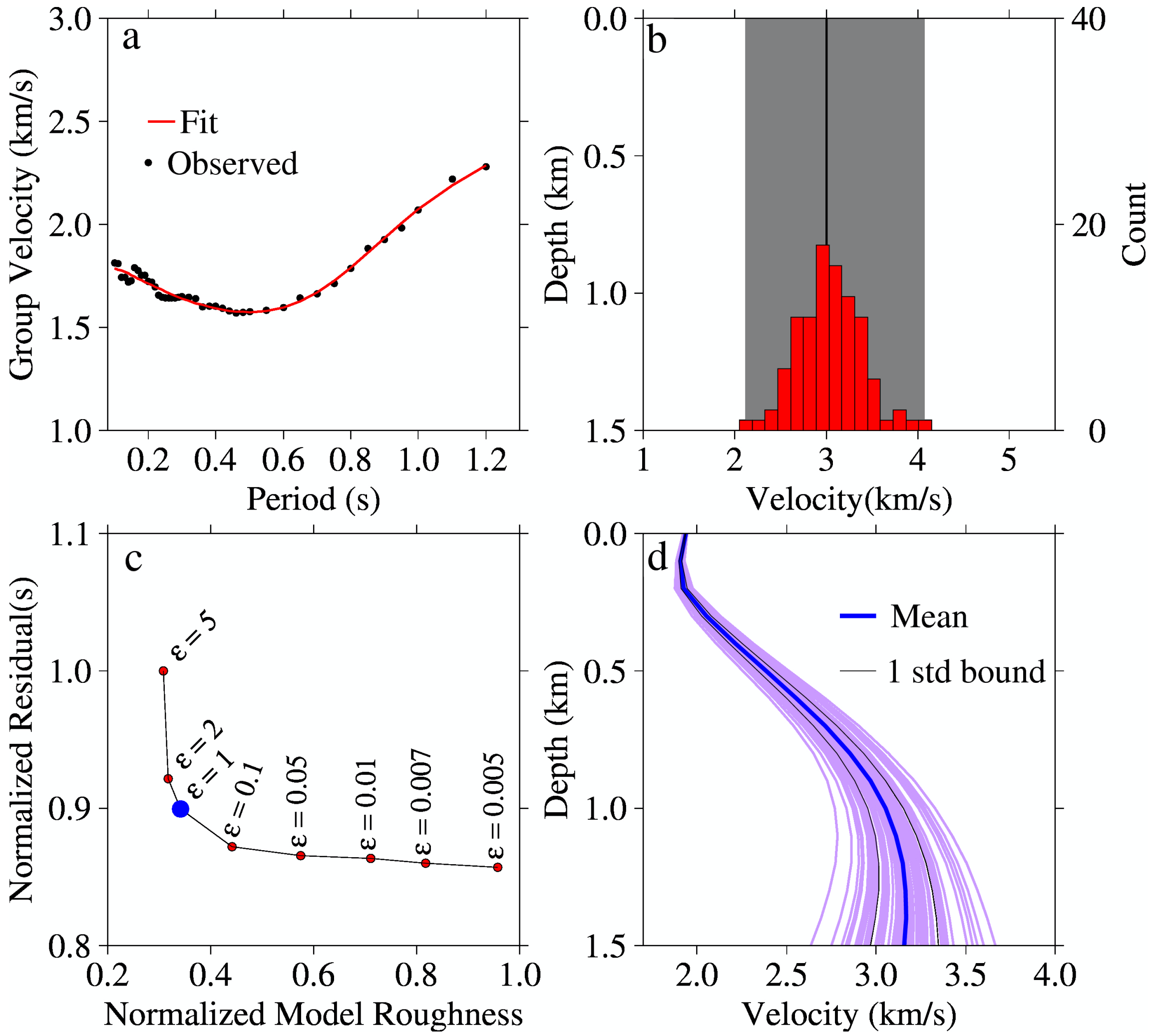

Figure S12. Same as Figure S7. The inversion is performed with a high damping value of 1 as shown in (c).

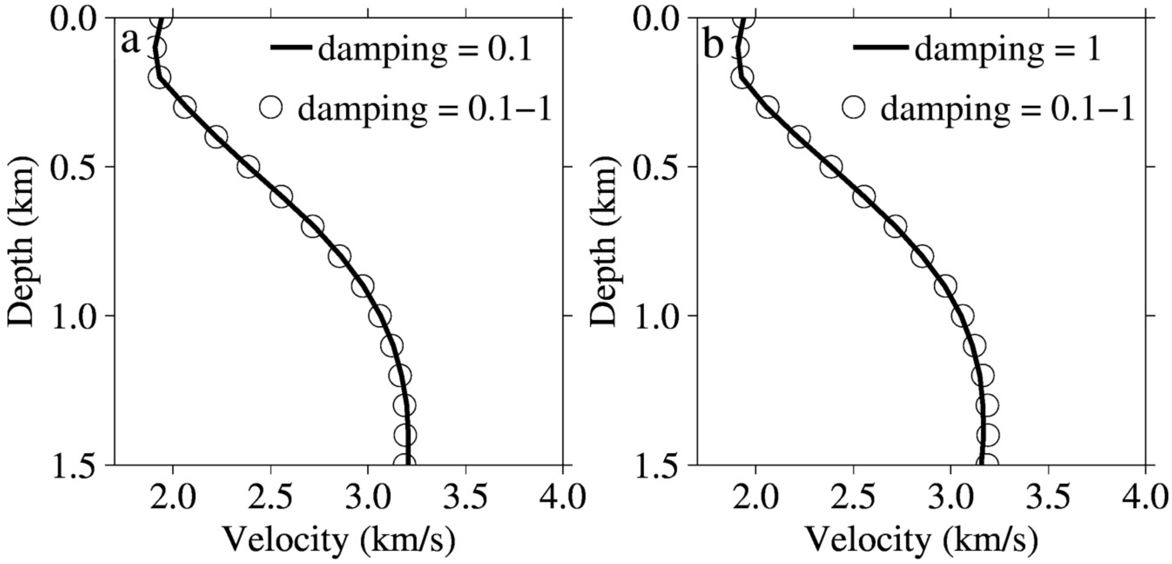

Figure S13. Comparison of the mean velocity model obtained after inversion with different damping parameters between 0.1 and 1, as shown in Figure S7, with that obtained at (a) a low damping value of 0.1 and (b) a high damping value of 1.

Station	Latitude	Longitude	Elevation
L01	19.932	76.596	527.0
L02	19.968	76.537	572.0
L03	19.980	76.519	608.0
L04	19.986	76.499	596.0
L05	19.974	76.480	565.0
L06	19.984	76.450	543.0
L07	20.005	76.410	554.0
L08	20.005	76.456	567.0
L09	19.967	76.506	597.0
L10	19.956	76.492	544.0
L11	19.952	76.484	552.0
L12	20.009	76.493	590.0
L13	20.033	76.532	540.0
L14	19.992	76.557	589.0
L15	20.017	76.556	574.0
L16	19.996	76.576	574.0
L17	19.953	76.566	532.0
L18	19.934	76.536	558.0
L19	19.936	76.492	539.0
L20	19.998	76.517	589.0

Table S1. Details of the seismic station used in the study.

Data set S1. Seismic waveform of ambient noise cross-correlations, group velocity data, and shear wave velocity data at each grid node used in the study are provided. The ambient noise waveform is in SAC (Seismic Analysis Code) format. The dispersion file is marked as Long_Lat.disp, and the shear wave velocity file is marked as Long_Lat.vel. Each file of the group velocity dispersion has two columns with period in first and group velocity in second. The velocity file has depth, mean velocity, median velocity, and standard deviation in its columns. Note that the shear wave velocity model is created using a set of 1000 models following the repeated inversion scheme.